

## Dynamical Mass Estimates of the $\beta$ Pictoris Planetary System Through Gaussian Process Stellar Activity Modelling

THOMAS VANDAL <sup>1,2</sup> JULIEN RAMEAU <sup>3,1</sup> AND RENÉ DOYON <sup>1</sup>

<sup>1</sup>*Institut de Recherche sur les Exoplanètes, Département de physique, Université de Montréal, CP 6128 Succ. Centre-ville, H3C 3J7, Montréal, QC, Canada*

<sup>2</sup>*Department of Physics, McGill University, 3600 rue University, H3A 2T8, Montréal, QC, Canada*

<sup>3</sup>*Université Grenoble Alpes/CNRS, Institut de Planétologie et d'Astrophysique de Grenoble, 38000 Grenoble, France*

(Received June 30, 2020; Accepted September 17, 2020)

Submitted to AJ

### ABSTRACT

Nearly 15 years of radial velocity (RV) monitoring and direct imaging enabled the detection of two giant planets orbiting the young, nearby star  $\beta$  Pictoris. The  $\delta$  Scuti pulsations of the star, overwhelming planetary signals, need to be carefully suppressed. In this work, we independently revisit the analysis of the RV data following a different approach than in the literature to model the activity of the star. We show that a Gaussian Process (GP) with a stochastically driven damped harmonic oscillator kernel can model the  $\delta$  Scuti pulsations. It provides similar results as parametric models but with a simpler framework, using only 3 hyperparameters. It also enables to model poorly sampled RV data, that were excluded from previous analysis, hence extending the RV baseline by nearly five years. Altogether, the orbit and the mass of both planets can be constrained from RV only, which was not possible with the parametric modelling. To characterize the system more accurately, we also perform a joint fit of all available relative astrometry and RV data. Our orbital solutions for  $\beta$  Pic b favour a low eccentricity of  $0.029^{+0.061}_{-0.024}$  and a relatively short period of  $21.1^{+2.0}_{-0.8}$  yr. The orbit of  $\beta$  Pic c is eccentric with  $0.206^{+0.074}_{-0.063}$  with a period of  $3.36 \pm 0.03$  yr. We find model-independent masses of  $11.7 \pm 1.4$  and  $8.5 \pm 0.5 M_{\text{Jup}}$  for  $\beta$  Pic b and c, respectively, assuming coplanarity. The mass of  $\beta$  Pic b is consistent with the hottest start evolutionary models, at an age of  $25 \pm 3$  Myr. A direct direction of  $\beta$  Pic c would provide a second calibration measurement in a coeval system.

**Keywords:** planets and satellites: detection, methods: statistical, stars: individual ( $\beta$  Pictoris)

### 1. INTRODUCTION

Exoplanets directly detected must rely on theoretical models to determine their masses from their luminosity and age. Not only is age difficult to evaluate (Soderblom et al. 2014), but evolutionary models are also uncalibrated at young ages ( $\leq 1$  Gyr) and low masses ( $\leq 70 M_{\text{Jup}}$ ). Model-independent mass measurements must be obtained to test these models, which ultimately will provide confidence in inferred masses for all directly imaged planets. Absolute astrometry with exquisite precision is amenable to achieve this goal.

Doppler spectroscopy of planet host stars can also determine the planet masses, biased with the orbit inclination which can be constrained from relative astrometry to overcome this bias. However, directly imaged planets are usually found at long periods around young stars since they are bright and spatially resolved with current instruments (see Bowler et al. 2014, and references therein). Radial velocity (hereafter RV) data must therefore be obtained over a long timescale. These data are however severely plagued by strong stellar activity signal due to spots, plagues, and pulsations (Galland et al. 2005; Lagrange et al. 2013; Hillenbrand et al. 2015). Planet detection is thus very challenging on both observational and data analysis sides. However, these limitations are less severe for low-mass star and high-mass

brown-dwarf companions to stars, enabling independent mass and luminosity measurements using a combination of relative, absolute astrometry, and/or radial velocity data. Evolutionary model calibration is therefore being undertaken for these objects. (Crepp et al. 2012; Ryu et al. 2016; Dupuy & Liu 2017). In the planetary mass regime, reduced signal amplitudes (RV, astrometry, contrast) make this task much harder.

$\beta$  Pictoris (hereafter  $\beta$  Pic) is a nearby ( $19.44 \pm 0.05$  pc, van Leeuwen (2007)), A6V (Gray et al. 2006), intermediate-mass ( $1.80^{+0.03}_{-0.04} M_{\odot}$  Wang et al. (2016)) star.  $\beta$  Pic has been classified as a  $\delta$  Scuti variable (Koen 2003) characterized by pulsation frequencies in the range 22.81-75.68 d<sup>-1</sup> (Mékarnia et al. 2017; Zwintz et al. 2019; Zieba et al. 2019).  $\beta$  Pic is a member of the  $\beta$  Pictoris moving group (Zuckerman et al. 2001), with recent age estimates of  $24 \pm 3$  Myr (Bell et al. 2014) and  $26 \pm 3$  Myr (Nielsen et al. 2016) using isochrones fitting, or  $25 \pm 3$  Myr by measuring the lithium depletion boundary on group members (Messina et al. 2016).  $\beta$  Pic is surrounded by a complex environment. The large circumstellar disk of gas and debris (Smith & Terrile 1984; Dent et al. 2013) has a primary component seen almost edge-on and an inner warp component tilted by  $+4.0 \pm 0.6^{\circ}$  and further inclined by  $6 \pm 1^{\circ}$  (Burrows et al. 1995; Mouillet et al. 1997; Golimowski et al. 2006; Ahmic et al. 2009; Lagrange et al. 2012b). Falling evaporating bodies or exocomets were evidenced (Lagrange et al. 1996; Kiefer et al. 2014; Zieba et al. 2019). Both warp and comets were modelled with gravitational perturbations by planet(s) within the system (Beust et al. 1990; Beust & Morbidelli 1996; Beust et al. 1998; Mouillet et al. 1997). Two giant planets were discovered within the system:  $\beta$  Pic b by direct imaging (Lagrange et al. 2010) and  $\beta$  Pic c with RV (Lagrange et al. 2019a). Monitoring the stellar RVs since 2008 (2003) up to 2018 combined with a multiparametric sinusoidal fit for the  $\delta$  Scuti pulsations led to a residual noise of 10 m s<sup>-1</sup>, allowing for the detection of  $\beta$  Pic c. The system is therefore a rare case for which independent mass measurement can be foreseen, as well as a deep understanding of a complex planetary system.

Simultaneous imaging of  $\beta$  Pic b and the disk proved that  $\beta$  Pic b is not coplanar with the main disk but consistent for being responsible for the inclined warp (Lagrange et al. 2012b). Monitoring the motion of  $\beta$  Pic b with direct imaging has led to various constraints on its orbit. The inclination is now well constrained, excluding perfectly edge-on orbit, at  $i = 89.04 \pm 0.04^{\circ}$  (Wang et al. 2016; Lagrange et al. 2019b; Nielsen et al. 2020; Nowak et al. 2020). Period and eccentricity were also constrained with direct imaging. Lagrange et al.

(2019b) reported  $P_b = 20.29^{+0.86}_{-1.35}$  yr and  $e_b = 0.01^{+0.03}_{-0.01}$  when using relative astrometric data only from VLT instruments (NaCo, SPHERE) while Nielsen et al. (2020) obtained  $P_b = 21.3^{+2.2}_{-1.0}$  yr and  $e_b = 0.038^{+0.063}_{-0.029}$  with all relative astrometric measurements except those from VLT/SPHERE. However, the inclusion of absolute astrometry from *Hipparcos* and *Gaia* in the analysis by Nielsen et al. (2020) lead to significantly higher period and eccentricity values, namely  $P_b = 24.4^{+1.0}_{-1.5}$  yr and  $e_b = 0.12^{+0.04}_{-0.03}$ . An analysis of the absolute astrometric motion of the star allowed Snellen & Brown (2018) to directly measure a planetary mass of  $M_b = 11 \pm 2 M_{\text{Jup}}$ ; Dupuy et al. (2019) found a mass of  $M_b = 13 \pm 3 M_{\text{Jup}}$  with additional corrections to the same data and further including relative astrometry and radial velocity data and fitting as well for the mass of the star. Analysis of the stellar RVs using VLT relative astrometric priors yielded  $M_b \sim 10 M_{\text{Jup}}$  (Lagrange et al. 2019a). Lastly, a joint analysis of direct imaging, RV and astrometric data accounting for both planets resulted in a mass of  $8.0 \pm 2.6 M_{\text{Jup}}$  for  $\beta$  Pic b (Nielsen et al. 2020). This is lower than previous estimate, but still consistent within  $1\sigma$ . These last two mass measurements account for the presence of a second giant planet in the system. The addition of a VLTI/GRAVITY relative astrometric point with exquisite precision of 80  $\mu$ as, but without the RVs and without accounting for a second planet, led Nowak et al. (2020) to measure  $M_b = 12.7 \pm 2.2 M_{\text{Jup}}$  while excluding circular orbit ( $e_b = 0.15^{+0.05}_{-0.04}$ ).

From stellar RVs only, the mass and period of  $\beta$  Pic c were estimated to  $M_c \sim 8.9 M_{\text{Jup}}$  (assuming the same inclination as  $\beta$  Pic b) and  $P_c \sim 1220$  d (Lagrange et al. 2019a), while Nielsen et al. (2020) found  $M_c = 9.18^{+0.96}_{-0.87} M_{\text{Jup}}$ ,  $P_c = 1238^{+7}_{-11}$  d, and  $e_c = 0.24^{+0.11}_{-0.10}$ .

RV data are therefore of prime importance when fitting for the masses of both planets, the absolute astrometry being still plagued by imperfect knowledge, bias, and required corrections of *Gaia* DR2 data onto bright stars (Brown et al. 2018). For  $\beta$  Pic, the  $\delta$  Scuti pulsations result in RV noise with a semi-amplitude of  $\sim 500$  m s<sup>-1</sup>, while  $\beta$  Pic b and c have expected semi-amplitudes of  $K_b \sim 70$  m s<sup>-1</sup> and  $K_c \sim 120$  m s<sup>-1</sup>, respectively. The main challenge is therefore to properly model and subtract the stellar activity, thus revealing planetary signals in the RV data.

A useful and increasingly used method to mitigate the stellar noise in the RV data of an active star is to use Gaussian processes (GP). There are several successful attempts to use this method in the literature (e.g., Haywood et al. (2014); Grunblatt et al. (2015); Cloutier et al. (2017b,a)). However, these examples are generally limited to less massive stars from the field for which the

stellar activity has fewer components and less temporal variations than for young stars like  $\beta$  Pic.

Here, we investigate possible improvements of the modelling of stellar activity in the RV data of  $\beta$  Pic in a Bayesian framework. We explore GPs for correlated Gaussian noise modelling over traditional parametric approaches from the literature (Lagrange et al. 2019a). This investigation leads to a measurement of the orbits and masses of both  $\beta$  Pic b and c from RV data only, an improvement over the literature that was unable to constrain the orbital parameters and mass of  $\beta$  Pic b from solely the same data. We then present a new joint analysis of all RV and astrometric data available, including RV points between 2003 and 2008 that were previously ignored in the literature. This analysis leads to new mass estimates for both planets.

The paper is structured as follows. Section 2 gives an overview of all archival data used for the analysis. In § 3, we outline the main elements of the GP method used to define a new stellar activity model for  $\beta$  Pic, followed in § 4 by a detailed orbit fitting analysis using RV alone, then adding astrometry data. A discussion of these results is presented in § 5 followed by a summary and conclusions in § 6.

## 2. LITERATURE DATA

In this work, we made use of published data that monitored the system over nearly the last 15 years. We were agnostic to the type and origin of the data but deliberately excluded absolute astrometric measurements from *Gaia*. Their analysis requires multiple known correction factors to compensate the star being very bright for the instrument (Brown et al. 2018) but also still unknown analysis steps to provide accurate measurements. We defer their inclusion into this type of work once the *Gaia* data release will be secured for bright stars.

### 2.1. ASTEP Photometry Timeseries

We had access to 6 358 photometric observations of  $\beta$  Pic from the Antarctica Search for Transiting Extrasolar Planets (ASTEP) 400 mm telescope (Crouzet et al. 2018), obtained between 7 and 13 June 2017 (JD = 2 457 910 to JD = 2 457 917), with a sampling rate of  $\sim 1000 \text{ d}^{-1}$  (Mékarnia et al. 2017, private communication). This light curve is shown in Figure 1, along with a GP fit explained in § 3.1. These observations were part of a longer monitoring campaign of  $\beta$  Pic (March to September 2017, Mékarnia et al. 2017). For this longer light curve, a periodogram analysis allowed Mékarnia et al. (2017) to detect 31  $\delta$  Scuti pulsation modes and to model the photometric stellar activity as a sum of sine waves. Since all of the 31 detected frequencies were

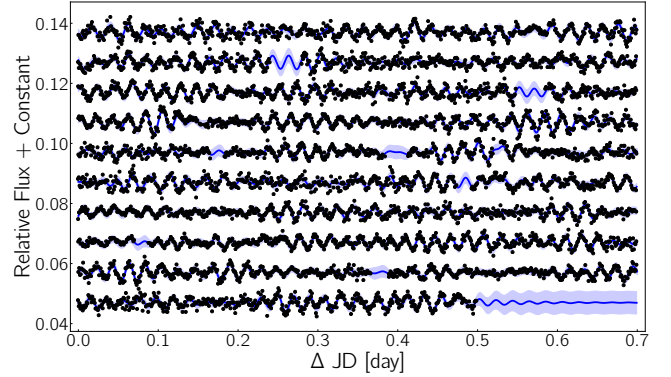


**Figure 1.** ASTEP photometric light curve of  $\beta$  Pic. The black dots are the observations between 7 (top left) and 13 (bottom right) June 2017. The data is split in segments of length  $\Delta\text{JD} = 0.7$  day and a constant offset is added to each segment to show the pulsations clearly. The solid blue line is the fit from an SHO GP and the shaded area is the  $1\sigma$  confidence interval.

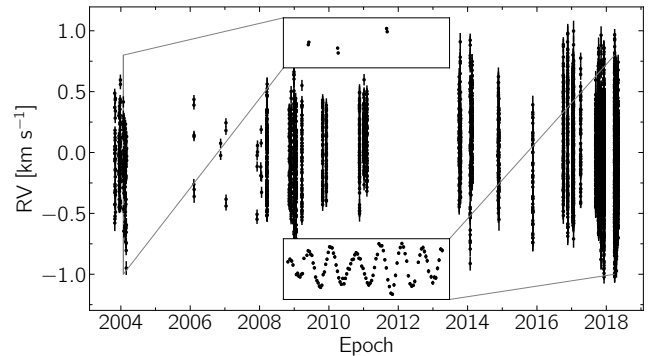


**Figure 2.** HARPS RV timeseries of  $\beta$  Pic. The inset on the bottom shows an example of the pulsations causing the high-amplitude noise in the RV data. The top inset shows how the sparse pre-2008 sampling hides these pulsations.

in the  $34.76\text{--}75.68 \text{ d}^{-1}$  interval, the fact that we only had access to a small portion of the photometric time series (6.8 d) should not prevent us from characterizing the activity of the star.

### 2.2. HARPS RV Timeseries

Lagrange et al. (2012a, 2019a) presented 5362 radial velocity measurements of  $\beta$  Pic obtained with the High Accuracy Radial velocity Planet Searcher (HARPS, Mayor et al. (2003)). These RV measurements, shown in Figure 2 and not corrected for stellar activity, were computed with the SAFIR package (Galland et al. 2005). These measurements, taken between October 2003 and May 2018, were sampled with two different methods. The sampling is much denser after March 2008, and reveals high-frequency variations in the RV data, with a similar timescale to the  $\delta$  Scuti pulsations detected

in the photometry (§ 2.1), that were not visible before that date (Lagrange et al. 2012a). The two insets in Figure 2 show example of these two different sampling methods (pre-2008 and post-2008). The poor sampling from before 2008 needs to be considered carefully when analyzing this data, especially if we attempt to model the high-frequency stellar activity in the radial velocities. One option is to neglect pre-2008 data and use only the well-sampled post-2008 data (Lagrange et al. 2019a; Nielsen et al. 2020). However, the observation baseline of the RV data is shorter than the period of  $\beta$  Pic b, so 5 additional years of data, leading to more than 14 years of RV coverage, would provide valuable information about the system. This is addressed in § 3.2, where we discuss the inclusion of pre-2008 data.

### 2.3. Relative Astrometry

We use all relative astrometry data available for  $\beta$  Pic. This includes nine epochs from VLT/NaCo (Lagrange et al. 2010; Currie et al. 2011; Chauvin et al. 2012), seven epochs from Gemini-South/NICI (Nielsen et al. 2014), two epochs from Magellan/MagAO (Morzinski et al. 2015), fifteen epochs from Gemini-South/GPI (Wang et al. 2016; Nielsen et al. 2020) and twelve epochs from VLT/SPHERE (Lagrange et al. 2019b). These measurements are all shown in Figure 10.

We also include the single epoch of relative astrometry obtained with VLTI/GRAVITY by Nowak et al. (2020) on September 22 2018. This data point, obtained by averaging 17 exposure files, is given by the bivariate normal distribution  $(\Delta RA, \Delta DEC) \sim \mathcal{N}(\boldsymbol{\mu}, \boldsymbol{\Sigma})$ .  $\boldsymbol{\mu}$  is the mean relative planet-to-star position and  $\boldsymbol{\Sigma} = \text{Cov}(\Delta RA, \Delta DEC)$ , the covariance matrix of all exposure files, gives the  $1\sigma$  confidence interval. The mean coordinates and their covariance, as reported by Nowak et al. (2020), are

$$\begin{cases} \boldsymbol{\mu} = \begin{bmatrix} \Delta RA \\ \Delta DEC \end{bmatrix} = \begin{bmatrix} 68.48 \\ 128.31 \end{bmatrix} \text{mas} \\ \boldsymbol{\Sigma} = \begin{bmatrix} 0.0027 & -0.0035 \\ -0.0035 & 0.0045 \end{bmatrix} \text{mas}^2. \end{cases} \quad (1)$$

This yields a precision more than an order of magnitude better than the other relative astrometry measurements mentioned above. The GRAVITY data point is shown in the inset of Figure 10.

## 3. STELLAR ACTIVITY MODELLING

### 3.1. ASTEP Photometry

Mékarnia et al. (2017) detected 31  $\delta$  Scuti pulsation frequencies between 34.76 and 75.68 d<sup>-1</sup> in the ASTEP

photometric light curve of  $\beta$  Pic, with a peak at 47.43 d<sup>-1</sup> (period of 30.4 min.). Similar high-frequency pulsations appear in the RV data (Lagrange et al. 2012a, 2019a), and their amplitude is far greater than the expected signals from  $\beta$  Pic b and c. Efficiently modelling and removing this stellar activity in the RV data is crucial if we intend to detect Keplerian planetary signals. Since the RV and photometric datasets exhibit similar pulsation patterns, we first train a null-mean GP on the ASTEP photometry. We use the *celerite* Python package (Foreman-Mackey et al. 2017) to compute the GP models used in the following analysis. To obtain posterior distributions of the GP hyperparameters, we use the affine-invariant Markov chain Monte-Carlo (MCMC) sampler from *emcee* (Foreman-Mackey et al. 2013). We use 128 walkers and ensure that all chains are longer than 40 times the integrated autocorrelation time. Once we have a distribution of the GP hyperparameters from photometry, we can apply it as a prior when fitting stellar activity in the RV data.

We first explore the use of a Quasi-Periodic (QP) kernel typically employed to model stellar rotation for stars quieter than  $\beta$  Pic (Haywood et al. 2014; Rajpaul et al. 2015; Grunblatt et al. 2015; Cloutier et al. 2017b; Angus et al. 2018). We refer to Foreman-Mackey et al. (2017) for an explicit definition of the QP kernel, both in the *celerite* framework (Equation 56) and in its more classical form (Equation 55). We find that this kernel is able to properly model the pulsations of  $\beta$  Pic, recovering the main period with  $P = 30.4$  min.

Foreman-Mackey et al. (2017) introduced a covariance function that represents a stochastically driven damped simple harmonic oscillator (SHO). This kernel is defined as:

$$k_{\text{SHO}}(\tau; S_0, Q, \omega_0) = S_0 \omega_0 Q \exp\left(-\frac{\omega_0 \tau}{2Q}\right) \times \begin{cases} \cosh(\eta \omega_0 \tau) + \frac{1}{2\eta Q} \sinh(\eta \omega_0 \tau), & 0 < Q < 1/2 \\ 2(1 + \omega_0 \tau), & Q = 1/2 \\ \cos(\eta \omega_0 \tau) + \frac{1}{2\eta Q} \sin(\eta \omega_0 \tau), & Q > 1/2 \end{cases}, \quad (2)$$

where  $\eta = |1 - (4Q^2)^{-1}|^{1/2}$ ,  $\omega_0$  is the frequency of the undamped oscillator,  $Q$  is the quality factor and  $S_0$  is proportional to the power at  $\omega = \omega_0$ ,  $S(\omega_0) = \sqrt{2/\pi} S_0 Q^2$ .  $\tau = |t_n - t_m|$  is the absolute time difference between any two observations taken at times  $t_n$  and  $t_m$ . When varying the quality factor, the SHO GP can provide an effective model for a large variety of phenomena. In the large  $Q$  limit, it can mimic quasi-periodic pulsations. Moreover, the spectrum of



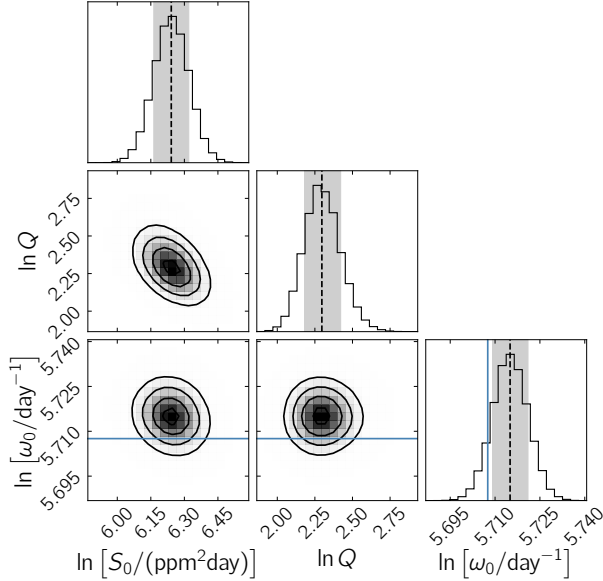


**Figure 3.** Posterior distribution of the SHO GP hyperparameters from the fit on the ASTEP photometry. Broad, uniform priors were used on all three hyperparameters. The dashed lines and grey shaded areas show the median and the  $1\sigma$  interval for each hyperparameter. The solid blue line shows the main frequency detected by Mékarnia et al. (2017).

an SHO covers a certain range of frequencies that depends on its hyperparameters. This ability to account for a wide range of frequencies provides some physical justification to adopt such a kernel in the context of a pulsating star like  $\beta$  Pic.

We find that the SHO GP models the  $\delta$  Scuti pulsations of  $\beta$  Pic adequately, yielding an  $\omega_0$  value corresponding to  $P \sim 30$  min. The posterior distribution of hyperparameters is shown in Figure 3. We note that the BIC favours the SHO kernel to the QP kernel very strongly, with  $\Delta\text{BIC} = 227$ .

We consider both kernels in the following analysis of the RV data since both sampling and baseline are different from that of the light curve, possibly affecting their responses to the fit.

### 3.2. HARPS RV

Typically, when a GP is used to model stellar activity in RV data, the GP and the Keplerian orbits are jointly fit, i.e. the mean function of the GP is the Keplerian model and they are modelled all at once on the entire dataset. This method has been successfully used in the past (e.g. Haywood et al. (2014); Rajpaul et al. (2015); Grunblatt et al. (2015); Cloutier et al. (2017b)). However, the stars studied were typically much quieter than  $\beta$  Pic. For this reason, we investigate an alternative approach similar to the one used by Lagrange et al.

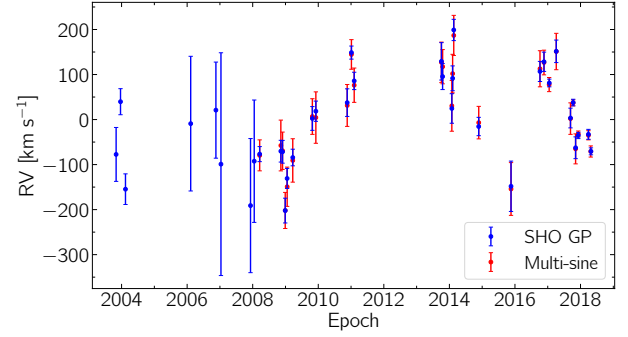


**Figure 4.** RV offsets for each group. The multi-sine offsets from Lagrange et al. (2019a) are shown in red and the SHO GP offsets from this work are shown in blue. All values for post-2008 offsets are consistent within  $1\sigma$  and the uncertainties on the GP offsets tend to be smaller than on the multi-sine ones by a factor of 1.5.

(2019a): we model the activity locally by splitting the data into subsets corresponding to continuous observing sequences (hereafter referred to as groups). Within these groups the maximum time separation between observations is 8 days. For each group, we use a GP model trained on the photometry, i.e. using posterior distributions from photometry as priors, with a constant mean. By letting all parameters vary in our MCMC, i.e. the GP hyperparameters and the constant mean, we can obtain an offset with an uncertainty (from the MCMC posterior distribution) for each group. These offsets thus represent the RV of the star at each epoch, and we can then fit them with a Keplerian model.

As mentioned in § 2.2, there is RV data available from 2003 to 2018. However, before 2008, the sampling is too sparse to exhibit the pulsations in the RV data. For this reason, Lagrange et al. (2019a) used only the data from after 2008. We note that using a multi-sine parametric model fitted on the well-sampled post-2008 groups to fit groups from before 2008 is not possible because of temporal variations in phase and amplitude of the pulsation modes. A GP, on the other hand, does not retain any phase information and is not strongly affected by small changes in the amplitude of individual modes. Therefore, only the covariance properties of the pulsations matter for a given GP to effectively model various epochs. We use a GP to model all available RV data between 2003 and 2018. After splitting the data as described above, we obtain 36 groups: the same 28 post-2008 groups as Lagrange et al. (2019a), and 8 additional pre-2008 groups. We then fit each group with a GP model previously trained on the photometry. To define the prior on the GP hyperparameters in the RV analysis, we use a kernel density estimate (KDE) of the posterior distributions from the photometry model (Fig-

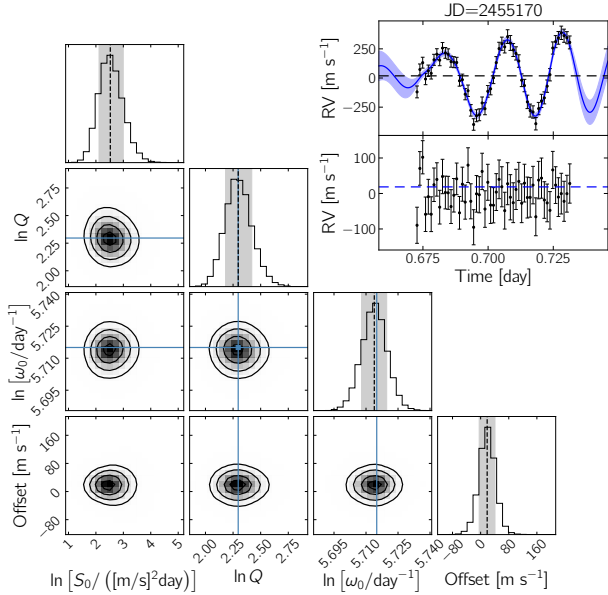


**Figure 5.** Example fit and posterior distribution for the SHO GP on RV Group #15. The dashed lines and grey shaded areas show the median and the  $1\sigma$  interval for each parameter (the three GP hyperparameters, and a constant offset). The solid blue lines show the median value of the training distribution for hyperparameters that were trained on the photometry. For  $S_0$  and the RV offset, broad uniform priors were used. In the top right corner, the GP fit of the RV data in Group #7 is shown as a solid blue line, with a shaded area showing the  $1\sigma$  confidence interval. The bottom panel shows the residuals, the dashed blue line being the resulting offset of the group.

ure 3 for the SHO GP). We do not use such a prior for the offset and the amplitude, which are both expected to vary between the two datasets.

We first test the QP kernel,  $k_{QP}$ , which properly accounts for the pulsations, but yields a large uncertainty on the RV offset. The uncertainties on RV offsets obtained with this kernel are approximately 4 times greater than those from the multi-sine parametric model used by Lagrange et al. (2019a).

The SHO kernel, on the other hand, results in offsets consistent with those from the multi-sine model, as shown in Figure 4. It yields uncertainties about 1.5 times smaller, while requiring 3 hyperparameters instead of up to 90 parameters (a sum of up to 30 sine waves with 3 parameters each, Lagrange et al. (2019a)). We also note that the RMS of the residuals from the SHO GP fit for all groups combined (with the offset subtracted from each group) is smaller by a factor of 1.4 than the RMS of the multi-sine residuals published by Lagrange et al. (2019a). The SHO GP thus provides an effective alternative to the multi-sine model. The posterior distribution of the three GP hyperparameters and

the constant offset, as well as the stellar activity fit for group # 15 (December 4 2009), are shown in Figure 5 as an example. Similar fits are obtained for the other groups and the hyperparameters are approximately constant throughout the groups, always staying within  $1\sigma$  of other groups and of the training values. No long term drift is thus further introduced with the modelling. This is also true for the poorly sampled pre-2008 groups.

Both the QP and SHO GPs were a priori reasonable models for the pulsations of  $\beta$  Pic. However, since the SHO GP is favoured by the BIC and also yields a better RV precision, we use RV offsets from this model in the remaining analysis.

#### 4. ORBIT FITTING

The stellar activity signal has been effectively corrected from the RV, enabling to fit the two-planets from the RV offsets in order to constrain their orbital parameters and masses. In this section, we first explore the information content of the RV alone. Our goal is to assess whether our extended baseline and increased precision can lead to any constraint on the two planets. Then, we make use of all observables of the two planets in addition to the RVs, including relative astrometry from the ground using adaptive optics and interferometric data, in a joint fit. This complete analysis will provide robust constraints on the planet parameters.

##### 4.1. RV Offsets Only

We perform a two-planet fit of the RV offsets using the `radvel` Python package (Fulton et al. 2018), along with `emcee` (Foreman-Mackey et al. 2013) for MCMC sampling. To evaluate the impact of the extended RV baseline and the sensitivity to priors from relative astrometry, we explore five different Cases. In all Cases, we use uniform or log-uniform priors for the parameters of  $\beta$  Pic c. For each planet, unless specified otherwise, we adjust five free parameters: the period  $P$ , the time of conjunction  $T_c$ ,  $h = \sqrt{e} \cos \omega$ ,  $k = \sqrt{e} \sin \omega$ , and the RV semi-amplitude  $K$ . We also fit for a global RV offset  $\gamma$  since the RVs were computed with respect to a reference spectrum (Galland et al. 2005; Lagrange et al. 2019a). We use the alternative parameters  $h$  and  $k$  because they reduce the correlation between eccentricity  $e$  and argument of periastron  $\omega$ <sup>1</sup> while also reducing the bias of the MCMC towards high eccentricities (Ford 2006). Additionally, we use the time of conjunction  $T_c$  instead of the time of periastron  $T_p$  since it is well defined for circular and low-eccentricity orbits.

The five cases are the following:

<sup>1</sup> In `radvel`,  $\omega$  is the argument of periastron of the star's orbit.

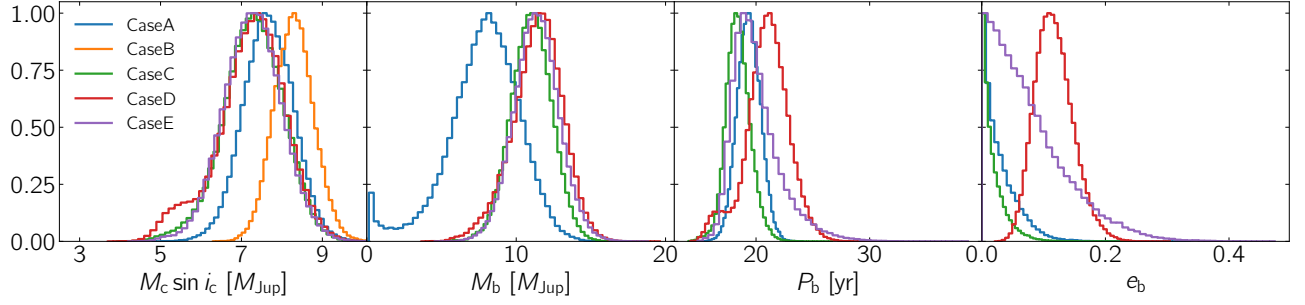


**Figure 6.** Posterior distribution for the minimum mass of  $\beta$  Pic c, the mass, the period and the eccentricity of  $\beta$  Pic b from the fit on RV data only. In Case B, only  $M_c \sin i_c$  was fitted among these parameters. Fixing the orbit and mass of  $\beta$  Pic b yields a greater, more precise mass for  $\beta$  Pic c (Case B). Using post-2008 data only yields less precise constraints on the mass of  $\beta$  Pic b with a small bimodality near  $M_b = 0 M_{\text{Jup}}$ . Including pre-2008 data refines the constraints on the mass of  $\beta$  Pic b, but its eccentricity and period are sensitive to the choice of priors. When a wide Gaussian prior is used on  $P_b$  and a uniform prior is used on  $e_b$  (Case E), low eccentricity and period are favoured.

- Case A. We consider only the post-2008 RV offsets, obtained with the SHO GP. We impose Gaussian priors on the orbital parameters of  $\beta$  Pic b based on the results from Lagrange et al. (2019b). This is similar to the analysis from Lagrange et al. (2019a), but we use Bayesian priors instead of repeating the fit with fixed orbital parameters randomly drawn from the prior for  $\beta$  Pic b.
- Case B. This is similar to Case A but we fix the orbital parameters of  $\beta$  Pic b to the best-fit values from Lagrange et al. (2019b) and its mass to  $10 M_{\text{Jup}}$ . As mentioned above, for each fit performed in Lagrange et al. (2019a), the orbital parameters of  $\beta$  Pic are fixed to randomly drawn values from direct imaging results.  $M_b$  was also held fixed, when using RV offsets only, and not all RV residuals. Case B is thus very close to the analysis from (Lagrange et al. 2019a) and enables a direct comparison of the parameters of  $\beta$  Pic c between their analysis and ours.
- Case C. Here, we include all available RV offsets between 2003 and 2018, obtained with the SHO GP. The 8 additional RV offsets described in § 3.2 provide an RV baseline of approximately 14 years. We use Gaussian priors from Lagrange et al. (2019b) on all parameters of  $\beta$  Pic b except its period and its mass. For  $M_b$ , we use a wide Jeffreys priors, and for  $P_b$ , we apply a Gaussian prior centred at 22 yr with  $\sigma = 4$  yr. This prior includes all period estimates published by Lagrange et al. (2019b) ( $\sim 20$  yr) and Nielsen et al. (2020) ( $\sim 24$  yr) within  $1\sigma$ .
- Case D. This is the same as Case C, but the priors from Lagrange et al. (2019b) are replaced with the

slightly different priors from Nielsen et al. (2020) to test the sensitivity of the posteriors.

- Case E. To test whether the extended RV data can reveal a change in eccentricity as it did for the period, we use a different parametrization of the Keplerian. Adjusting the parameters  $P$ ,  $T_c$ ,  $e$ ,  $\omega$  and  $K$ , which is already implemented in `radvel`, simplifies the use a uniform prior on  $e_b$  while imposing a Gaussian prior on  $\omega$ , whose value is consistent in both Lagrange et al. (2019b) and Nielsen et al. (2020).

For each case, the adopted priors and the median of the parameter posterior distributions, along with the  $1\sigma$  uncertainties corresponding to the 16th and 84th percentiles, are summarized in Table 1. We also report the Bayesian Information Criterion (BIC) for each case to facilitate model comparison. Here, we provide an overview of the main results.

As mentioned above, Lagrange et al. (2019a) used all of the RV residuals for each group between 2008 and 2018 to constrain the mass of  $\beta$  Pic b. When only the multi-sine offsets are used, the mass of  $\beta$  Pic b is not constrained and has to be held fixed. In Case A, thanks to the increased precision provided by the SHO GP, we constrain the orbital parameters and masses of both planets using the 28 RV offsets only. We find  $M_b = 8.0^{+2.1}_{-2.4} M_{\text{Jup}}$  and  $M_c = 7.7 \pm 0.6 M_{\text{Jup}}$ . These masses are both lower than those found by Lagrange et al. (2019a). As shown in Figure 6, the posterior distribution of  $M_b$  includes a small bimodality near  $0 M_{\text{Jup}}$ . The results from this fit should therefore be interpreted carefully.

In Case B, we obtain results consistent with those of Lagrange et al. (2019a) and Nielsen et al. (2020) for the orbital parameters and the mass of  $\beta$  Pic c. The main difference is in eccentricity, with  $e = 0.161^{+0.064}_{-0.057}$  being lower than values from the literature, but still consistent

Table 1. Two-Planet Fit With RV Data Only

	Case A		Case B		Case C		Case D		Case E (Adopted - RV Only) 2003-2018	
	2008-2018	2003-2018	2008-2018	2003-2018	2003-2018	2003-2018	2003-2018	2003-2018	2003-2018	2003-2018
	Prior	Posterior	Prior	Posterior	Prior	Posterior	Prior	Posterior	Prior	Posterior
$P_b$ [yr] <sup>a</sup>	$\mathcal{N}(20.3, 1.1)$	$19.4 \pm 1.0$	Fixed to 20.3	$\mathcal{N}(22, 4)$	$\mathcal{N}(22, 4)$	$18.4^{+1.1}_{-1.0}$	See C	$21.1 \pm 1.8$	See C	$19.6^{+2.4}_{-1.5}$
$T_{c,b}$ [JD-2 450 000]	$\mathcal{N}(8010, 15)$	$8012 \pm 15$	Fixed to 8010	See A	See A	$8013 \pm 15$	See A	$8013 \pm 15$	See A	$8012 \pm 15$
$h_b = \sqrt{e_b} \cos \omega_b$ <sup>b</sup>	$\mathcal{N}(0.09, 0.10)$	$0.14 \pm 0.10$	Fixed to 0.09	See A	See A	$0.10 \pm 0.09$	$\mathcal{N}(0.33, 0.05)$	$0.32 \pm 0.05$	—	—
$k_b = \sqrt{e_b} \sin \omega_b$	$\mathcal{N}(0.03, 0.04)$	$0.03 \pm 0.04$	Fixed to 0.03	See A	See A	$0.03 \pm 0.04$	$\mathcal{N}(0.11, 0.03)$	$0.10 \pm 0.3$	—	—
$K_b$ [m s <sup>-1</sup> ]	$\mathcal{J}^*(1, 200)$	$58^{+15}_{-17}$	Fixed to 69.4	See A	See A	$81 \pm 10$	See A	$81^{+10}_{-11}$	See A	$82 \pm 10$
$e_b$	—	$0.021^{+0.035}_{-0.017}$	Fixed to 0.010	—	—	$0.013^{+0.023}_{-0.010}$	—	$0.115^{+0.033}_{-0.028}$	$\mathcal{U}(0.0, 0.5)$	$0.062^{+0.075}_{-0.044}$
$\omega_b$ [deg]	—	$13^{+31}_{-15}$	Fixed to 20	—	—	$16^{+49}_{-21}$	—	$17^{+6}_{-5}$	$\mathcal{N}(20, 10)$	$16 \pm 11$
$a_b$ (AU)	—	$8.7 \pm 0.3$	Fixed to 9.1	—	—	$8.4^{+0.4}_{-0.3}$	—	$9.2 \pm 0.5$	—	$8.8^{+0.7}_{-0.5}$
$M_b$ [M <sub>Jup</sub> ]	—	$8.0^{+2.1}_{-2.4}$	Fixed to 10.0	—	—	$11.0 \pm 1.4$	—	$11.5^{+1.6}_{-1.8}$	—	$11.4 \pm 1.5$
$P_c$ [yr] <sup>a</sup>	$\mathcal{U}(2.74, 3.83)$	$3.29 \pm 0.03$	See A	$3.32 \pm 0.03$	See A	$3.32^{+0.03}_{-0.04}$	See A	$3.32^{+0.04}_{-0.05}$	See A	$3.32 \pm 0.04$
$T_{c,c}$ [JD-2 450 000]	$\mathcal{U}(7500, 9000)$	$8118^{+32}_{-33}$	See A	$8152^{+23}_{-20}$	See A	$8141^{+29}_{-28}$	See A	$8141^{+31}_{-35}$	See A	$8143^{+31}_{-28}$
$h_c = \sqrt{e_c} \cos \omega_c$ <sup>b</sup>	$\mathcal{U}(-1, 1)$	$0.11^{+0.18}_{-0.17}$	See A	$0.04 \pm 0.12$	See A	$0.03 \pm 0.14$	See A	$0.04^{+0.16}_{-0.15}$	—	—
$k_c = \sqrt{e_c} \sin \omega_c$	$\mathcal{U}(-1, 1)$	$-0.23^{+0.27}_{-0.16}$	See A	$-0.38^{+0.10}_{-0.08}$	See A	$-0.34^{+0.19}_{-0.12}$	See A	$-0.32^{+0.28}_{-0.13}$	—	—
$K_c$ [m s <sup>-1</sup> ]	$\mathcal{J}^*(1, 200)$	$101 \pm 8$	See A	$110 \pm 7$	See A	$96 \pm 10$	See A	$96^{+10}_{-11}$	See A	$96 \pm 10$
$e_c$	—	$0.111^{+0.082}_{-0.061}$	—	$0.161^{+0.064}_{-0.057}$	—	$0.141^{+0.084}_{-0.076}$	—	$0.138^{+0.102}_{-0.081}$	See A	$0.130^{+0.083}_{-0.080}$
$\omega_c$ [deg]	—	$-64^{+75}_{-34}$	—	$-84^{+20}_{-17}$	—	$-84^{+34}_{-23}$	—	$-81^{+67}_{-25}$	$\mathcal{U}(0, 0.99)$	$-84^{+38}_{-25}$
$a_c$ [AU]	—	$2.68 \pm 0.03$	—	$2.69 \pm 0.02$	—	$2.69 \pm 0.03$	—	$2.69 \pm 0.03$	$\mathcal{U}(-200, 160)$	$2.69 \pm 0.03$
$M_c \sin i_c$ [M <sub>Jup</sub> ]	—	$7.7 \pm 0.6$	—	$8.3 \pm 0.5$	—	$7.3 \pm 0.8$	—	$7.3^{+0.8}_{-0.9}$	—	$7.3 \pm 0.8$
$\gamma$ [m s <sup>-1</sup> ]	$\mathcal{U}(-100, 100)$	$-21 \pm 9$	See A	$-31 \pm 5$	See A	$-26 \pm 9$	See A	$-33^{+12}_{-11}$	See A	$-30 \pm 10$
BIC <sup>c</sup>	383		367		496		500		498	

NOTE— $\mathcal{J}(a, b)$  denotes a Jeffrey's prior between  $a$  and  $b$ ,  $\mathcal{N}(\mu, \sigma)$  denotes a Gaussian prior,  $\mathcal{J}^*(k, m)$  denotes a modified Jeffrey's prior that behaves as a uniform below  $k$  and as a Jeffrey's prior between  $k$  and  $m$ .

<sup>a</sup>Periods are given in years for convenience, but the units used for the analysis were days.

<sup>b</sup>When fitting  $h_j$  and  $k_j$ , we also always ensure that  $e_j = h_j^2 + k_j^2 < 1$ .

<sup>c</sup>BIC values can only be compared when the two model fit the same values of independent variable, i.e. Case A and B should be compared separately from Cases C, D and E.



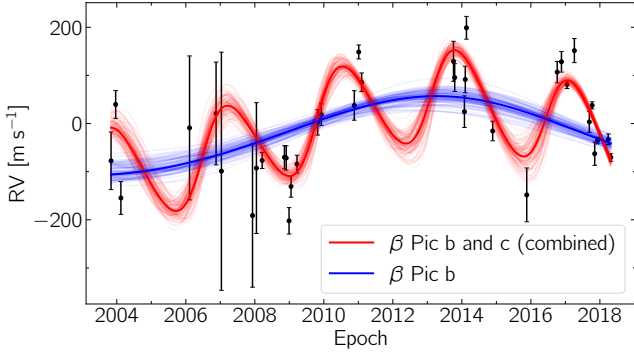


**Figure 7.** Example fit using RV data only. All RV offsets between 2003 and 2018 are shown in black. The fit of  $\beta$  Pic b and c combined is shown as a solid red line, and the corresponding solution for  $\beta$  Pic b only is shown in blue. Both are shown along with 100 random MCMC samples. This fit corresponds to Case E in Table 1

within  $2\sigma$ . This result suggests that the GP RV offsets might favor slightly lower eccentricities than multi-sine offsets from Lagrange et al. (2019a). The BIC for Cases A and B yield  $\Delta\text{BIC}_{A-B} = 16$ , providing very strong evidence in favour of Case B. This is mostly attributable to the difference in the number of parameters. The fact that allowing more free parameters does not yield better agreement with the data is another sign that parameters of  $\beta$  Pic b are not totally well-constrained by the 2008-2018 GP offsets only, and that results from Case A should be interpreted with caution. However, the fact that they enable constraints on the signal of  $\beta$  Pic b with RV offsets only does show that the smaller error bars of the GP offsets provide more information on the planetary orbits compared to the multi-sine offsets.

In Cases C and D, we first tried using uniform priors for the orbit of  $\beta$  Pic b, but several parameters were not constrained properly. Hence, as described above, we use Gaussian priors for all parameters of  $\beta$  Pic b except its mass. Performing a two-planet fit, we find  $P_b = 18.4^{+1.1}_{-1.0}$  yr for Case C and  $P_b = 21.1 \pm 1.8$  yr for Case D. Both Cases seem to favour lower periods than references from which the priors were taken, but are consistent with their respective reference within  $2\sigma$ . As shown in Figure 6, the eccentricity is also sensitive to the choice of priors with Case C allowing circular orbits and Case D favouring slightly eccentric orbits. The masses, on the other hand, show low sensitivity to the choice of priors. Case C yields  $[M_b, M_c] = [11.0 \pm 1.4, 7.3 \pm 0.8] M_{\text{Jup}}$  while Case D gives  $[M_b, M_c] = [11.5^{+1.6}_{-1.8}, 7.3^{+0.8}_{-0.9}] M_{\text{Jup}}$ . We note that the BIC values shown in Table 1 provides evidence in favour of Case C with priors from Lagrange et al. (2019b).

In Case E, we find  $P_b = 19.6^{+2.4}_{-1.5}$  yr and  $e_b = 0.062^{+0.072}_{-0.045}$ . Therefore, the RV data favours low period and circular orbits when these two parameters are not constrained ( $e_b$ ) or weakly constrained ( $P_b$ ) with priors from direct imaging. Constraints on both masses remain unaffected by this change of parametrization and priors (see Figure 6). Figure 7 shows the RV fit corresponding to Case E and Figure 8 shows the posterior distribution of the fitted parameters. The distributions are generally well-constrained. The apparent correlation between  $e_b$  and  $P_b$  is consistent with results from the literature where longer periods are generally associated with more eccentric orbits (Lagrange et al. 2019b; Nielsen et al. 2020; Dupuy et al. 2019). We note that the BIC favours Case E to Case D, but not Case C. In both cases, the evidence is only marginal with  $\Delta\text{BIC} = 2$ . This suggests that priors from astrometry can still provide valuable information about the orbit of  $\beta$  Pic b despite the better constraints provided by the GP offsets and the extended RV baseline.

Throughout the 5 Cases,  $\beta$  Pic c is always detected with a false-alarm probability  $\text{FAP} < 2.2 \times 10^{-6}$ , and its orbital parameters and its mass show very low sensitivity to the choice of orbital priors for  $\beta$  Pic b. The constraints on  $M_b$  are also unaffected by changes in these priors. As mentioned above, the improved precision of GP offset plays an important role in our ability to constrain  $M_b$  in Case A. However, one can clearly see in Figure 6 that the additional 2003-2008 RV coverage improves the mass estimate, yielding  $M_b = 11.4 \pm 1.5 M_{\text{Jup}}$  (Case E) and completely ruling out solutions where b is undetected. This mass is consistent with the indicative mass of  $M_b \sim 10 M_{\text{Jup}}$  reported by Lagrange et al. (2019a). Thanks to the extended RV baseline, we are now able to constrain the mass of both planets from RV data only with very good precision and low sensitivity to the choice of priors.

#### 4.2. RV Offsets and Relative Astrometry

To further assess the impact of the extended RV baseline and of the GP offsets, and to better characterize the system as whole, we perform a joint fit of all available RV and relative astrometry data. To do so, we still use `radvel`, but we include custom models and likelihoods to account for relative astrometry. We still rely on on the Keplerian solver from `radvel`, but we then derive values of Separation (Sep.) and position angle (PA) using a model similar to the one used in `orbitize!` (Blunt et al. 2020).

In this joint model, we fit the following orbital parameters for both planets: semimajor axis  $a$ , time of conjunction  $T_c$ ,  $h = \sqrt{e} \cos \omega$  and  $k = \sqrt{e} \sin \omega$ . To account

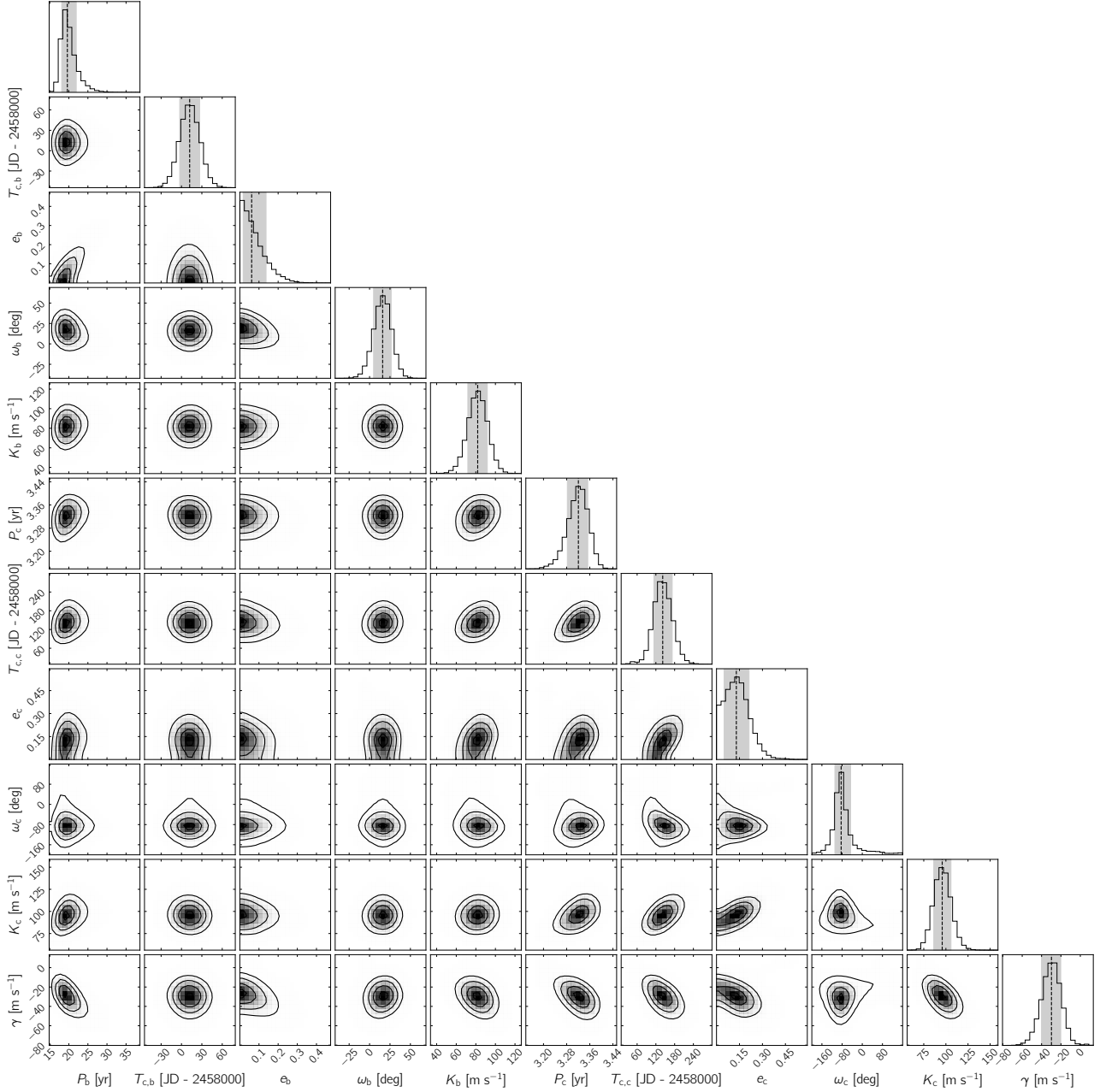


**Figure 8.** Posterior distribution of the Case E RV fit. The dashed lines and grey shaded areas show the median and the  $1\sigma$  interval for each parameter. Low-eccentricity orbits are preferred for  $\beta$  Pic b. This corresponds to shorter orbital periods due to the correlation between these two parameters.

for the relative astrometry of  $\beta$  Pic b, we also adjust its inclination  $i_b$ , the position angle of ascending node  $\Omega_b$ , the parallax  $\pi$  and the total mass  $M_{\text{Tot}}$ . Since the inclination of  $\beta$  Pic b is constrained by relative astrometry, we fit for its mass,  $M_b$ , directly. This is not the case of  $\beta$  Pic c so we use  $M_c \sin i_c$ . As in § 4.1, we also include a global RV offset  $\gamma$ . Finally, as pointed out by Nielsen et al. (2020), there is evidence for a systematic position angle offset between GPI and SPHERE. Following their analysis, we include two additional free parameters: a

multiplicative correction,  $\rho_S/\rho_G$ , in separation and an additive offset position angle,  $\theta_S - \theta_G$ , both applied to GPI data points. This adds up to a total of 17 free parameters. We use uniform or log-uniform priors on all parameters except the parallax for which we use a Gaussian prior corresponding to  $\pi = 51.44 \pm 12$  mas, as measured by *Hipparcos* (van Leeuwen 2007). For  $\Omega_b$ , we use a uniform prior between  $\pi/10$  and  $\pi/2$ , to account for the planetary RV measurement by Snellen et al. (2014). For the inclination, we use a prior uniform in  $\sin(i_b)$ .

**Table 2.** Two-Planet Joint Fit of RV and Relative Astrometry

	Joint Fit		Joint Fit With Gravity (Adopted - Final)	
	Prior	Posterior	Prior	Posterior
$P_b$ [yr]	—	$21.2^{+2.4}_{-0.9}$	—	$21.1^{+2.0}_{-0.8}$
$T_{c,b}$ [JD-2 450 000]	$\mathcal{U}(7000, 9000)$	$8012.2 \pm 2.3$	$\mathcal{U}(7000, 9000)$	$8011.2 \pm 0.5$
$h_b = \sqrt{e_b} \cos \omega_b$ <sup>a</sup>	$\mathcal{U}(-1, 1)$	$0.156^{+0.137}_{-0.175}$	$\mathcal{U}(-1, 1)$	$0.146^{+0.123}_{-0.160}$
$k_b = \sqrt{e_b} \sin \omega_b$ <sup>a</sup>	$\mathcal{U}(-1, 1)$	$0.074^{+0.061}_{-0.101}$	$\mathcal{U}(-1, 1)$	$0.077^{+0.058}_{-0.098}$
$e_b$	—	$0.033^{+0.069}_{-0.027}$	—	$0.029^{+0.061}_{-0.024}$
$\omega_b$ [deg]	—	$22^{+18}_{-67}$	—	$25^{+15}_{-62}$
$a_b$ [AU]	$\mathcal{J}(1, 100)$	$9.3^{+0.7}_{-0.3}$	$\mathcal{J}(1, 100)$	$9.2^{+0.6}_{-0.2}$
$M_b$ [ $M_{\text{Jup}}$ ]	$\mathcal{U}(1, 20)$	$11.8 \pm 1.4$	$\mathcal{U}(1, 20)$	$11.7 \pm 1.4$
$\Omega_b$ [deg]	$\mathcal{U}(18, 90)$	$32.07 \pm 0.08$	$\mathcal{U}(18, 90)$	$32.00^{+0.06}_{-0.05}$
$i_b$ [deg]	$\sin i$	$88.97 \pm 0.09$	$\sin i$	$88.88^{+0.04}_{-0.03}$
$P_c$ [yr] <sup>a</sup>	—	$3.36 \pm 0.03$	—	$3.36 \pm 0.03$
$T_{c,c}$ [JD-2 450 000]	$\mathcal{U}(7500, 9000)$	$8177^{+31}_{-27}$	$\mathcal{U}(7500, 9000)$	$8177^{+31}_{-27}$
$h_c = \sqrt{e_c} \cos \omega_c$ <sup>a</sup>	$\mathcal{U}(-1, 1)$	$0.024^{+0.102}_{-0.103}$	$\mathcal{U}(-1, 1)$	$0.025 \pm 0.103$
$k_c = \sqrt{e_c} \sin \omega_c$ <sup>a</sup>	$\mathcal{U}(-1, 1)$	$-0.442^{+0.085}_{-0.080}$	$\mathcal{U}(-1, 1)$	$-0.442^{+0.086}_{-0.081}$
$e_c$	—	$0.206^{+0.074}_{-0.063}$	—	$0.206^{+0.074}_{-0.063}$
$\omega_c$ [deg]	—	$-87^{+14}_{-13}$	—	$-87^{+14}_{-13}$
$a_c$ [AU]	$\mathcal{J}(2, 3.5)$	$2.71 \pm 0.02$	$\mathcal{J}(2, 3.5)$	$2.71 \pm 0.02$
$M_c \sin i_c$ [ $M_{\text{Jup}}$ ]	$\mathcal{U}(1, 20)$	$8.5 \pm 0.5$	$\mathcal{U}(1, 20)$	$8.5 \pm 0.5$
$M_{\text{Tot}}$ [ $M_{\odot}$ ]	$\mathcal{U}(1.4, 2.0)$	$1.76 \pm 0.03$	$\mathcal{U}(1.4, 2.0)$	$1.76 \pm 0.03$
$\pi$ [mas]	$\mathcal{N}(51.44, 0.12)$	$51.44 \pm 0.12$	$\mathcal{N}(51.44, 0.12)$	$51.44 \pm 0.12$
$\rho_S/\rho_G$	$\mathcal{U}(0.5, 1.5)$	$0.99 \pm 0.6$	$\mathcal{U}(0.5, 1.5)$	$0.99 \pm 0.6$
$\theta_S - \theta_G$ [deg]	$\mathcal{N}(0.0, 0.5)$	$-0.14 \pm 0.48$	$\mathcal{N}(0.0, 0.5)$	$-0.15 \pm 0.48$
$\gamma$ [ $\text{m s}^{-1}$ ]	$\mathcal{U}(-100, 100)$	$-42^{+7}_{-8}$	$\mathcal{U}(-100, 100)$	$-42 \pm 7$

<sup>a</sup>When fitting  $h_j$  and  $k_j$ , we also always ensure that  $e_j = h_j^2 + k_j^2 < 1$ .

A detailed list of adopted priors is provided in Table 2. We perform two joint fits: one with and one without the VLTI/GRAVITY data point from September 2018. The posterior distribution of all parameters for both fits is shown in Appendix A.

We perform a first fit using all available data except the GRAVITY measurement from 2018. In general, values are consistent with the RV-only fit, but have better precision. While constraints on the mass of  $\beta$  Pic b barely change with the inclusion of relative astrometry, yielding  $M_b = 11.8 \pm 1.4 M_{\text{Jup}}$ , the mass of  $\beta$  Pic c is now measured at  $M_c = 8.5 \pm 0.5 M_{\text{Jup}}$ , an increase of about  $1 M_{\text{Jup}}$  compared to the RV fits of § 4.1. This constraint on  $M_c$  is consistent with the literature (Lagrange et al. 2019a; Nielsen et al. 2020). However, accounting for  $\beta$  Pic c does not cause a decrease in  $M_b$  as reported by Nielsen et al. (2020) ( $\sim 8 M_{\text{Jup}}$ ) and, to a lesser extent, Lagrange et al. (2019a) ( $\sim 10 M_{\text{Jup}}$ ). This is likely due to the extended RV baseline, to the increased precision of the GP offsets compared to the multi-sine offsets,

to the fact that we do not include absolute astrometry, or to a combination of those 3 factors. The tendency towards short-period (20-21 yr), low-eccentricity orbits observed when fitting RV data only is confirmed in the joint fit, and both parameters are constrained more precisely, as shown in Figure 9. We note that the measured eccentricity of  $\beta$  Pic c is now slightly higher at  $e_c = 0.206^{+0.074}_{-0.063}$  and is in better agreement with the literature (Lagrange et al. 2019a; Nielsen et al. 2020). Similarly to Nielsen et al. (2020), we find no evidence of a systematic offset  $\rho_G/\rho_S$  in separation. In PA, however, the correction stays unconstrained after the MCMC has reached convergence. In an attempt to better constrain this parameter, we use a wide Gaussian prior centred at  $0^\circ$  with  $\sigma = 0.5^\circ$ . This prior includes the correction of  $-0.47^\circ \pm 0.14^\circ$  found by Nielsen et al. (2020) within  $1\sigma$ . We then find a correction  $\theta_G - \theta_S = -0.14^\circ \pm 0.48^\circ$ . This corresponds to a true north offset as reported by Nielsen et al. (2020), but the offset is smaller, and is consistent with  $0^\circ$  well within  $1\sigma$ . In addition, we per-

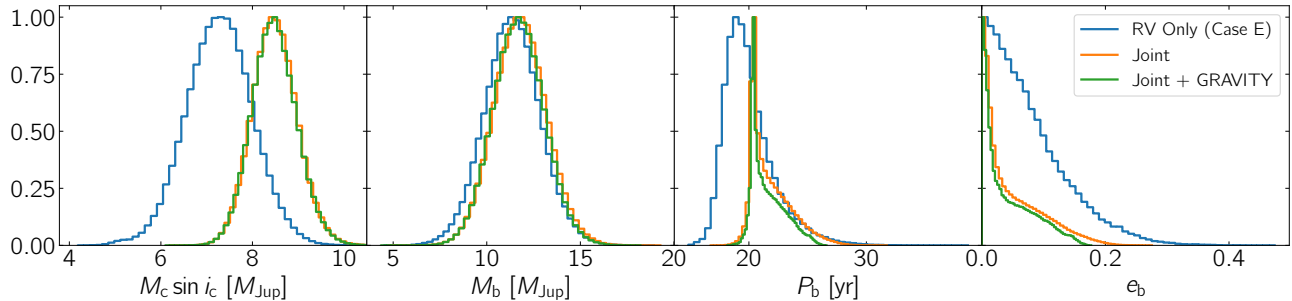


**Figure 9.** Posterior distribution for the minimum mass of  $\beta$  Pic c, the mass, the period and the eccentricity of  $\beta$  Pic b. The parameter distributions are shown for a fit of RV data only (Case E), a joint fit of RV data and relative astrometry, and the same joint fit, but including the high-precision measurement from VLTI/GRAVITY. The joint fit generally provides better precision than the RV-only fit. Low-eccentricity and short period orbits are also more strongly favoured. The inclusion of the GRAVITY measurement slightly improves the precision of most parameters, but does not cause a dramatic change in any of them.

formed a fit without including any correction and found that the posterior distribution of orbital parameters was unaffected.

When including the GRAVITY data point in our fit, we must add a second custom term to the log-likelihood since the two coordinates ( $\Delta\text{RA}$  and  $\Delta\text{DEC}$ ) are correlated. To do so, we first calculate the Pearson correlation coefficient corresponding to the covariance matrix of Equation 1. This allows us to obtain the probability density function (PDF) of a bivariate normal distribution centred on the model values, but with an analytical solution that does not require any matrix inversion, taking advantage of the pre-computed correlation coefficient. We then evaluate this PDF at the coordinates of the data point to obtain the likelihood before taking its logarithm and adding it to the other two likelihoods (RV and other relative astrometry). However, the covariance matrix  $\Sigma$  from Equation 1, reported by Nowak et al. (2020), is not positive semi-definite. This yields an invalid Pearson correlation coefficient  $r < -1$ . This issue is likely due to an approximation in the reported covariance matrix. We therefore simply set the off-axis elements of the covariance matrix to  $\sigma_{\Delta\text{RA},\Delta\text{DEC}} = \sigma_{\Delta\text{DEC},\Delta\text{RA}} = -0.00348 \text{ mas}^2$ . This small change of  $0.00002 \text{ mas}^2$  reestablishes the positive semi-definiteness of  $\Sigma$  and puts the Pearson coefficient back in the expected interval  $-1 < r < 1$ <sup>2</sup>. The principal components of this adjusted covariance matrix give the error bars on the GRAVITY measurement, as shown in the top left panel Figure 10. Once this fix is applied, we can fit for all available relative astrometry, including the GRAVITY measurement.

<sup>2</sup> Note that the original covariance matrix does not perfectly match the error bars shown in Figure 2 of Nowak et al. (2020) since both were made separately at different moments of the analysis and not updated for publication (J. Wang, private communication)

As reported in Table 2, the inclusion of the GRAVITY measurement yields results consistent with the joint fit performed without including it. However, in general, the precision is slightly improved when including the GRAVITY measurement, which is more precise than other relative astrometric measurements by more than an order of magnitude. This precision improvement is marginal and can thus hardly be seen by looking at the posterior distribution of parameters, but a careful inspection of Figure 9 does reveal a sharper peak in  $P_b$  and a slightly stronger preference for low-eccentricity orbits. Even when using relative astrometry only, Nowak et al. (2020) reported a preference for slightly eccentric orbits ( $e_b = 0.15^{+0.05}_{-0.04}$ ), which we do not observe here. This could be because they do not account for  $\beta$  Pic c in their analysis while we account for both planets using the RV offsets (see Hara et al. (2019) for a detailed discussion of such possible eccentricity biases). Figure 10 shows the joint fit of RV data with all available relative astrometry, including the GRAVITY measurement. The fit is in good agreement with the high-precision GRAVITY measurement, as shown in the top left panel.

## 5. DISCUSSION

The orbital properties and masses of  $\beta$  Pic b and c provide additional knowledge about the full planetary system architecture, including the debris disk, and its evolution with time. We discuss the impact of our findings on these two aspects and propose future directions to further improve the system characterization.

Our orbital parameters for  $\beta$  Pic b confirm that the planet is misaligned with the main disk and consistent with the inner warp Lagrange et al. (2012a). A direct detection of  $\beta$  Pic c would also provide a measurement of the inclination of its orbit, further revealing the inner architecture of the system with respect to the disk. We show the orbit of  $\beta$  Pic b to have a very small eccentricity ( $< 0.06$ ). This value is still consistent at  $1\sigma$  with the

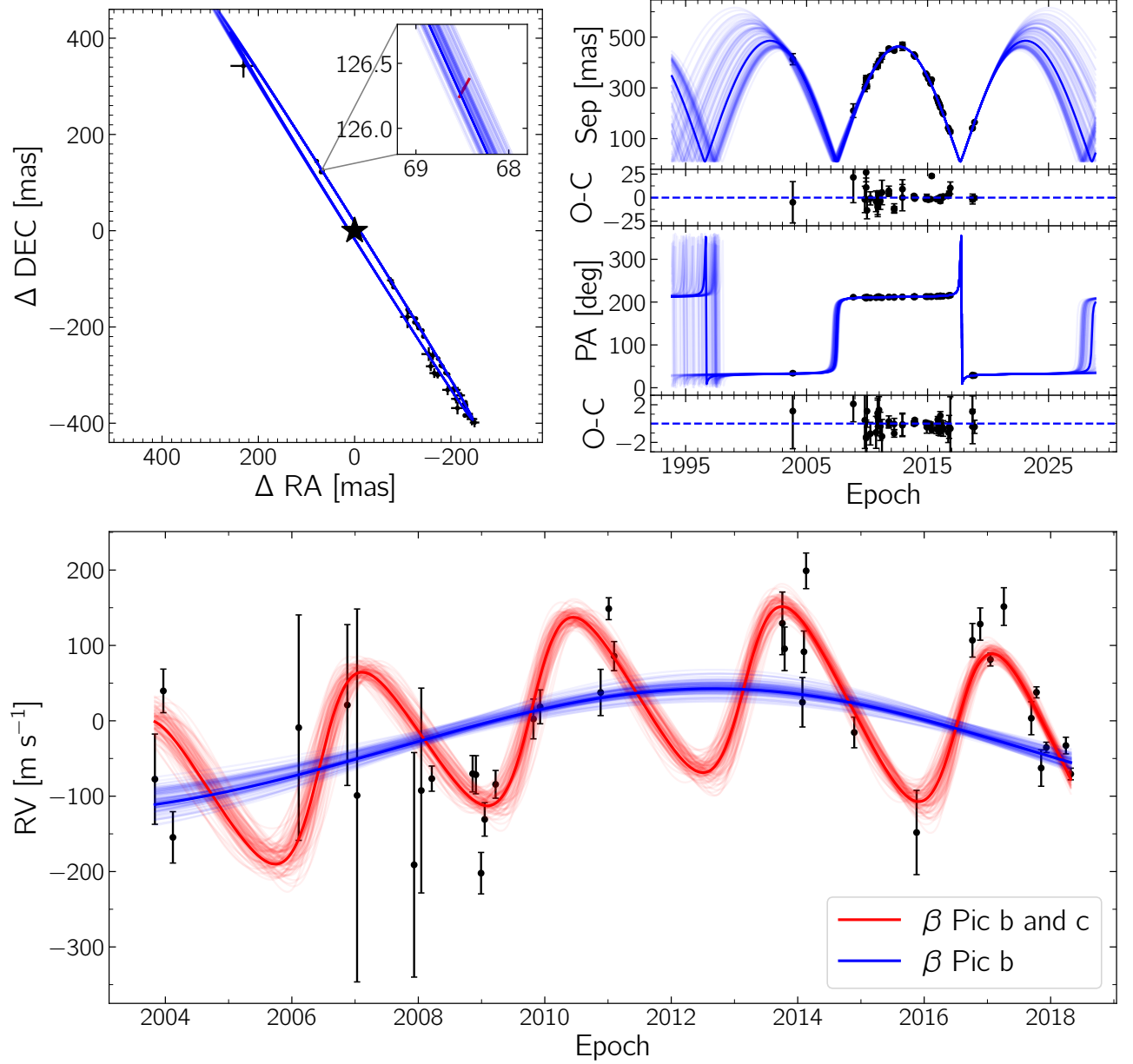


**Figure 10.** Joint fit of RV offsets with all available relative astrometry of  $\beta$  Pic b. In all panels, the orbit of  $\beta$  Pic b is shown in blue. In the top left panel, it is shown along with all relative astrometry measurements. The VLTI/GRAVITY measurement appears in an inset to show how its high precision constraints the fit. All other relative astrometry measurements were fit in separation and position angle rather than RA and DEC, as shown in the top right panel. The bottom panel shows the 36 RV offsets along with the joint signal of both planets in addition to the signal of  $\beta$  Pic b alone. All fits are shown with 100 random samples from the MCMC.

planet being responsible for the exocomets ( $e > 0.05$ ) (Beust & Morbidelli 1996), but the inclusion of the more eccentric orbit of  $\beta$  Pic c should be investigated.

The mass of directly-imaged planets cannot be obtained from direct spectrophotometric measurements. Without complementary data like RV or absolute astrometry, the estimate of this parameter solely relies on theoretical models, which predict the temporal evolu-

tion of the luminosity of a planet for a variety of masses. The ages of directly imaged planet hosts is usually well constrained (e.g. Mamajek & Bell 2014); the bolometric luminosity of the planets are computed from their spectral energy distributions. However, the evolutionary models are not calibrated at young ages ( $< 1\text{Gyr}$ ) and low masses ( $< 72M_{\text{Jup}}$ ). The model-based masses of the directly imaged planets might then be incorrect.



The independent mass measurement of  $\beta$  Pic b, derived from the RV data, offers a rare opportunity to be compared against the predictions of the evolutionary models. In the following, we will compute the predicted mass according to the known age and luminosity of  $\beta$  Pic b and see whether the modelled-derived age is consistent with our dynamical mass.

We considered the classical hot start evolutionary model grid COND (Baraffe et al. 2003)<sup>3</sup>, the recent hot start grid SONORA<sup>4</sup> (Marley et al. in prep.), and the warm-start grid from Spiegel & Burrows (2012). We use grids computed at solar metallicity since the metallicity of  $\beta$  Pic b is not well constrained from existing spectrophotometric data, with estimated values from  $-0.5$  up to  $0.63$  (Nowak et al. 2020), depending on the data and analysis method. The distributions of the predicted mass for all three evolutionary models were derived with a Monte Carlo process from the normal distributions of the most recent luminosity measurement for  $\beta$  Pic b of  $\log L/L_{\odot} = -3.76 \pm 0.02$  (Chilcote et al. 2017) and from the age of  $25 \pm 3$  Myr (Messina et al. 2016) (this age assumes  $\beta$  Pic b formed very quickly after the birth of the host star). The grid luminosity was first interpolated in  $\log t$ , at each randomly selected age, for each mass bin. The  $\log M$  was then interpolated in  $\log L_{\text{bol}}$  at each randomly selected luminosity to derive the model-dependent mass. The process was repeated  $10^5$  times to derive the distribution of the model-derived mass. Figure 12 shows the distributions for the three models, compared to our dynamical mass measurement. We found  $12.9^{+0.2}_{-0.3} M_{\text{Jup}}$ ,  $12.9 \pm 0.1 M_{\text{Jup}}$ , and  $13.6 \pm 0.1 M_{\text{Jup}}$  for the COND, SONORA and warm-start model at the highest available entropy,  $13 \text{ k}_{\text{B}}/\text{baryon}$ , following the analysis of Chilcote et al. (2017). The results are still consistent with Morzinski et al. (2015), Chilcote et al. (2017) and Nielsen et al. (2020), who used different age and/or luminosity estimates ( $23 \pm 3$  Myr,  $24 \pm 3$  Myr, and  $26 \pm 3$  Myr respectively, and  $\log L_{\text{bol}}/L_{\odot} = -3.78 \pm 0.03$ ). Mostly driven by the tight constraint on the bolometric luminosity, the model derived masses exhibit a precision ten times better than our dynamical mass measurement. Yet, the two cold-start model grids are consistent to better than  $1\sigma$  to our dynamical mass measurement and the warm-start model from Spiegel & Burrows (2012) is consistent within  $2\sigma$  at the measured age of the system, favouring formation with the highest initial entropy, following the same conclusion reached by Nielsen et al. (2020). Our precision is neither high enough to pre-

cisely calibrate the evolutionary tracks, nor to discriminate which of the hot start or warm-start scenarios best fit the parameters of  $\beta$  Pic b, nor to derive the age of the system assuming the models are accurate.

Alternatively, one can assume the evolutionary models predict correct masses for a given luminosity-age pair. Under such hypothesis, one can conversely use our dynamical mass measurement to determine any significant formation delay of  $\beta$  Pic b, with respect to A, according to its measured luminosity (Currie et al. 2009). However, the large uncertainty on the dynamical mass only translates into an upper limit on this delay of 12 Myr at  $1\sigma$  for all three evolutionary models, which is more than any timescale for giant planet formation. A precision of  $0.1 M_{\text{Jup}}$  is required to test this scenario.

A continuous and long term monitoring of  $\beta$  Pic b via relative and absolute astrometry, especially with the exquisite precision of VLTI/GRAVITY, and spectroscopy will enable to improve the orbital parameters and the mass precision to revisit the calibration of the evolutionary models and/or the formation delay hypothesis, following the same conclusions as Nielsen et al. (2020). As seen in Figure 11, a lot of orbital solutions for  $\beta$  Pic b would be excluded by a better constraint on its period. The fact that both relative astrometry and RV data cover less than a full period for  $\beta$  Pic leads to a greater uncertainty in  $P_{\text{b}}$ . Continuous monitoring of  $\beta$  Pic b in the next 5 years will strongly constrain maximum separation of  $\beta$  Pic b in the northeastern half of the orbit, hence enabling a better precision in  $P_{\text{b}}$ . Furthermore, continuous RV monitoring of  $\beta$  Pic as well as the use of unbiased absolute astrometric measurements from *Gaia* in combination with the long baseline with *Hipparcos* would not only help to constrain the period of  $\beta$  Pic b, but it would also improve the accuracy and precision of model-independent mass measurements for both planets.

Similarly, a direct detection of  $\beta$  Pic c together with an adequate sampling of its spectral energy distribution would provide another independent luminosity measurement within the same system, at a lower dynamical mass. This would further strengthen the tests of the evolutionary models. Direct imaging of  $\beta$  Pic c may be possible with the *James Webb Space Telescope* (JWST) or with next-generation giant ground based telescopes such as the European Extremely Large Telescope (E-ELT), which should provide an angular resolutions of  $\sim 100$  mas for the former and  $\sim 30$  mas for the latter. As shown in Figure 11, the separation between  $\beta$  Pic c and its host is greater than 100 mas for a significant fraction of its orbit according to the solutions derived in this work. Such a measurement would independently

<sup>3</sup> The most recent grid from Baraffe et al. (2015) does not reach a luminosity that is dim enough at the age of the system.

<sup>4</sup> 10.5281/zenodo.1309034

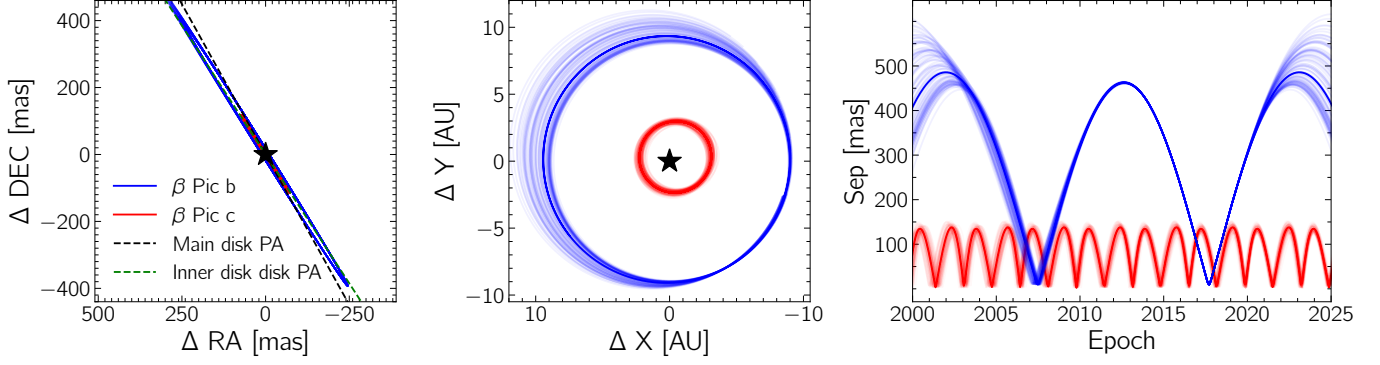


**Figure 11.** Orbit solutions showing the system architecture in various coordinates. The left panel shows the orbit of both planets in RA and DEC, assuming coplanar orbits for both planets. The planetary orbits are slightly inclined from the main disk in position angle (PA), but are almost aligned with the inner disk (Lagrange et al. 2012b). The middle panel shows both orbits as seen from the pole, with the orbit of  $\beta$  Pic b being nearly circular and the orbit of  $\beta$  Pic c slightly eccentric. The separation between both planets and the star is shown in the left panel. In all three panel, the orbit of  $\beta$  Pic b is shown in blue and that of  $\beta$  Pic c is in red, along with 100 random MCMC realisations. The main uncertainty in the trajectory of  $\beta$  Pic b appears to come from a lack of data in the northeastern part of its orbit, leading to a large range of possible orbital periods.

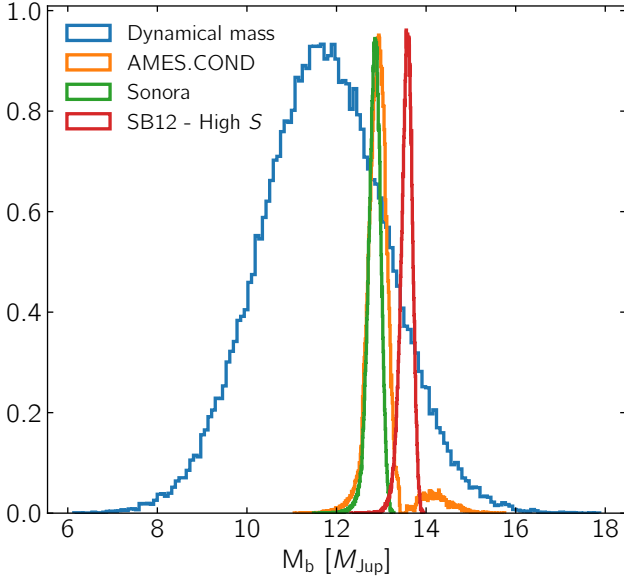


**Figure 12.** Distributions of the mass of  $\beta$  Pic b from our dynamical measurement (black) compared to predictions from the evolutionary models COND (Baraffe et al. 2003), SONORA (Marley et al. in prep) and the warm-start model with  $S = 13$  k<sub>B</sub>/baryon from Spiegel & Burrows (2012) assuming an age of  $25 \pm 3$  Myr (Messina et al. 2016) and a bolometric luminosity of  $\log L/L_{\odot} = -3.76 \pm 0.02$  (Chilcote et al. 2017).

confirm the existence of the planet while providing another measurement to calibrate mass-luminosity models.

## 6. CONCLUSION

We present a new and independent analysis of the RVs of  $\beta$  Pic. For the first time, we use a SHO GP framework to model the stellar activity of the star, with

a training of the model from the photometric lightcurve, which results in the following results:

- We show that the SHO GP enables to model the  $\delta$  Scuti pulsations with amplitudes as high as several hundreds of meters per second;
- It yields better precision than a QP kernel typically used to model stellar rotation and is favoured according to the BIC;
- It yields RV offsets consistent with parametric models from the literature (Lagrange et al. 2019a);
- It provides a simpler framework than the parametric models, with three hyperparameters instead of up to 90 parameters;
- It allows to model poorly sampled RVs, excluded from previous analyses, hence expanding the baseline by nearly 5 years, as early as 2003.

This extended RV coverage and the precision of the SHO GP offsets make it possible to constrain the mass of both planets using RV data only with low sensitivity to the choice of priors imposed on the orbit of  $\beta$  Pic b. However, the constraints on other orbital parameters are sensitive to changes in the priors from orbital fits using relative and absolute astrometry in the literature (Lagrange et al. 2019b; Nielsen et al. 2020). To better characterize the entire system, we also perform a fit of all available relative astrometry and RV data. The joint fits and the fits with RV data only yield results that are generally consistent. We find a model-independent mass of  $12.7 \pm 1.3 M_{\text{Jup}}$  for  $\beta$  Pic b. A low-eccentricity orbit ( $e = 0.016^{+0.044}_{-0.012}$ ) with a relatively short period of

$P_b = 20.6^{+1.5}_{-0.4}$  yr is preferred. For  $\beta$  Pic c, the mass is constrained to  $8.5 \pm 0.5 M_{\text{Jup}}$  and the orbit is consistent with values from the literature (Lagrange et al. 2019a; Nielsen et al. 2020).

The dynamical mass measurement of  $\beta$  Pic b presented in this work is consistent with hot-start and warm-start evolutionary models at the highest computed initial entropy ( $S = 13$  k<sub>B</sub>/baryon) but is not precise enough to discriminate against any of the models tested, reaching conclusions similar to Nielsen et al. (2020). Further monitoring with relative and absolute astrometry, as well as RV, will be required to obtain stronger constraints on the mass, enabling a better calibration of mass-luminosity models.

$\beta$  Pic c has not yet been observed directly, but according to the orbital solutions presented here, it could be accessible by direct imaging in the near future with *JWST*. With a minimum mass of  $8.5 \pm 0.5 M_{\text{Jup}}$ , the COND evolutionary model predicts a contrast with the star around 10.7 magnitudes and 8.9 magnitudes, at K-band and L-band respectively. Such a detection would provide a second point for calibration of evolutionary model while further improving the characterization of orbits in the  $\beta$  Pic system.

This work demonstrates that precise modelling of complex stellar activity with SHO GP is effective. It opens a new path towards the detection of giant planets with RV only around young stars as well as the characterization of systems with directly imaged planets beyond that of  $\beta$  Pic.

*Software:* emcee (Foreman-Mackey et al. 2013), celerite (Foreman-Mackey et al. 2017), RadVel (Fulton et al. 2018), Astropy (The Astropy Collaboration et al. 2013), corner (Foreman-Mackey 2016), orbitize! (Blunt et al. 2020).

## ACKNOWLEDGMENTS

We sincerely thank the referee for the thoughtful and careful review, and the suggestions, leading to an improvement of the present work. We thank Anne-Marie Lagrange for providing all published individual RV measurements and Djamel Mékarnia for the ASTEP light curve. We thank Lauren Weiss for her contribution to early phases of this project and Aurélien Wyttenbach and Raphalle Haywood for fruitful discussions about GP. TV acknowledges support from an Institut de Recherche sur les Exoplanètes (iREx) Trottier Excellence Grant. JR and RD acknowledge support from Fonds de Recherche du Québec since JR’s work was performed in part under contract with the University of Montréal. JR is supported by the French National Research Agency in the framework of the Investissements d’Avenir program (ANR-15-IDEX-02), through the funding of the ”Origin of Life” project of the Univ. Grenoble-Alpes.”

## APPENDIX

## A. POSTERIOR DISTRIBUTIONS FOR ALL FITS

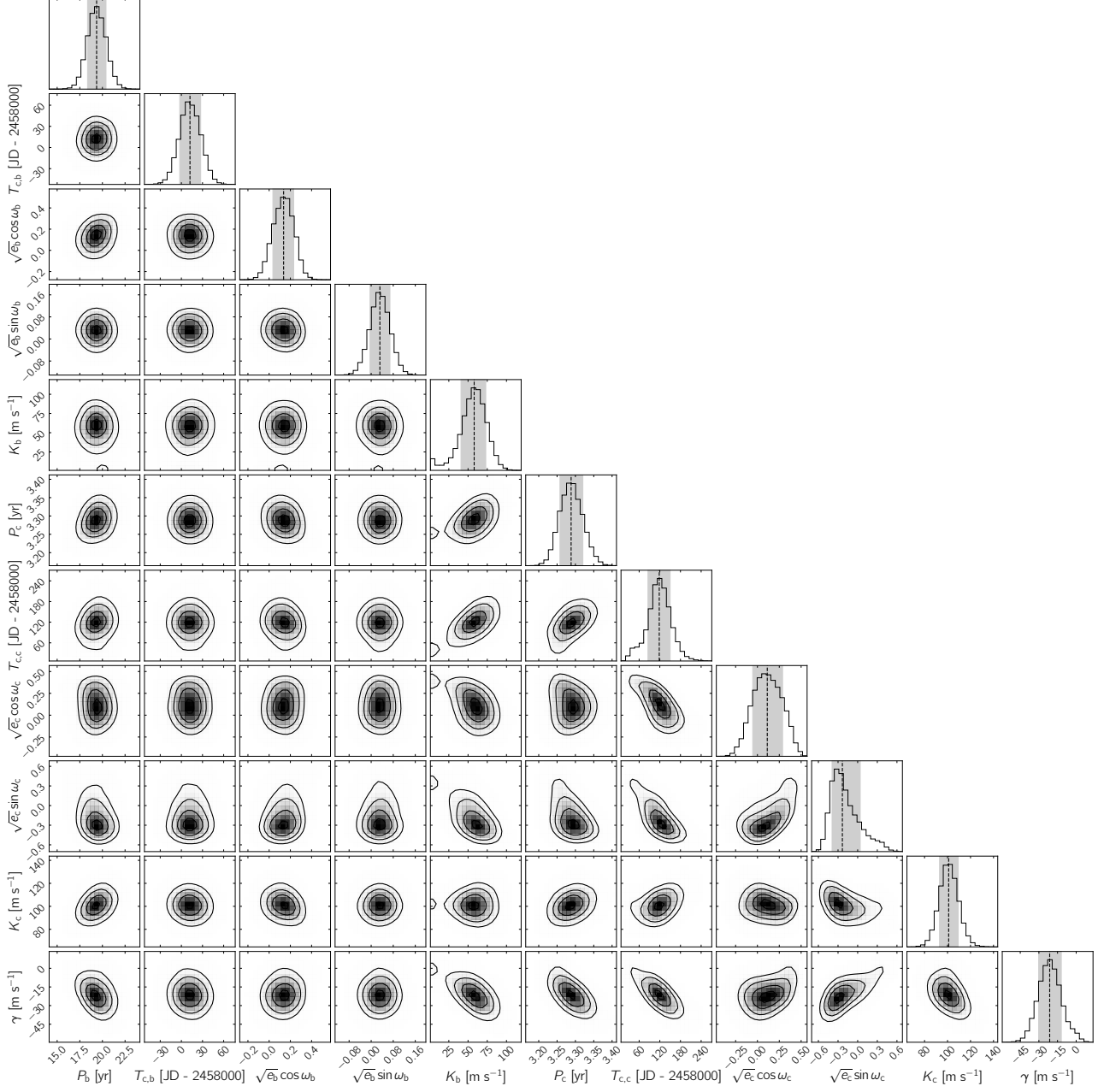


**Figure 13.** Posterior distribution of the Case A RV fit. The dashed lines and grey shaded areas show the median and the  $1\sigma$  interval for each parameter. A small bimodality in  $M_b$  suggests that the orbit of  $\beta$  Pic b is not totally well-constrained by the 2008-2018 RV offsets only.

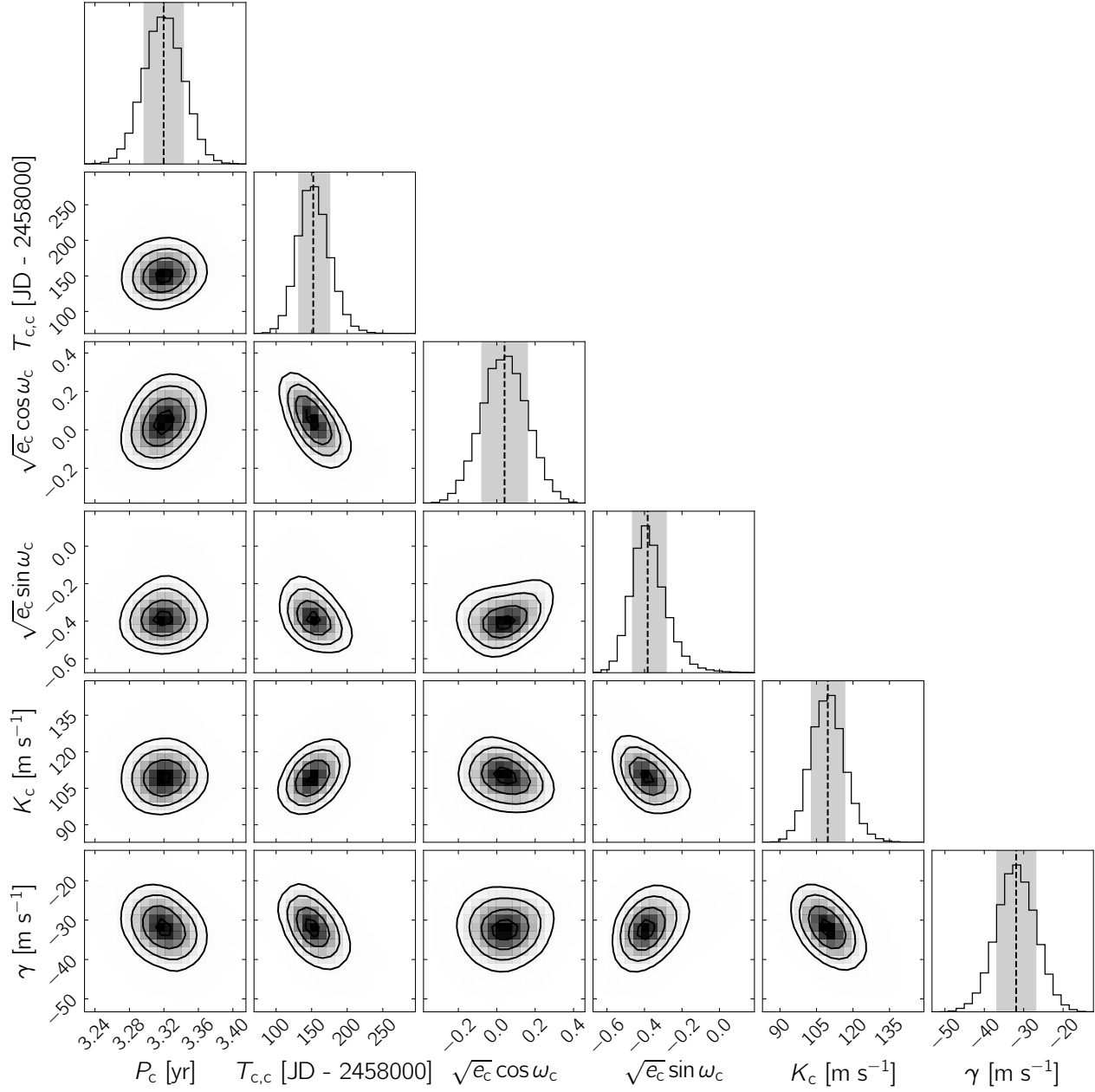


**Figure 14.** Posterior distribution of the Case B RV fit. The dashed lines and grey shaded areas show the median and the  $1\sigma$  interval for each parameter. The orbit of  $\beta$  Pic b is fixed to values from [Lagrange et al. \(2019b\)](#).



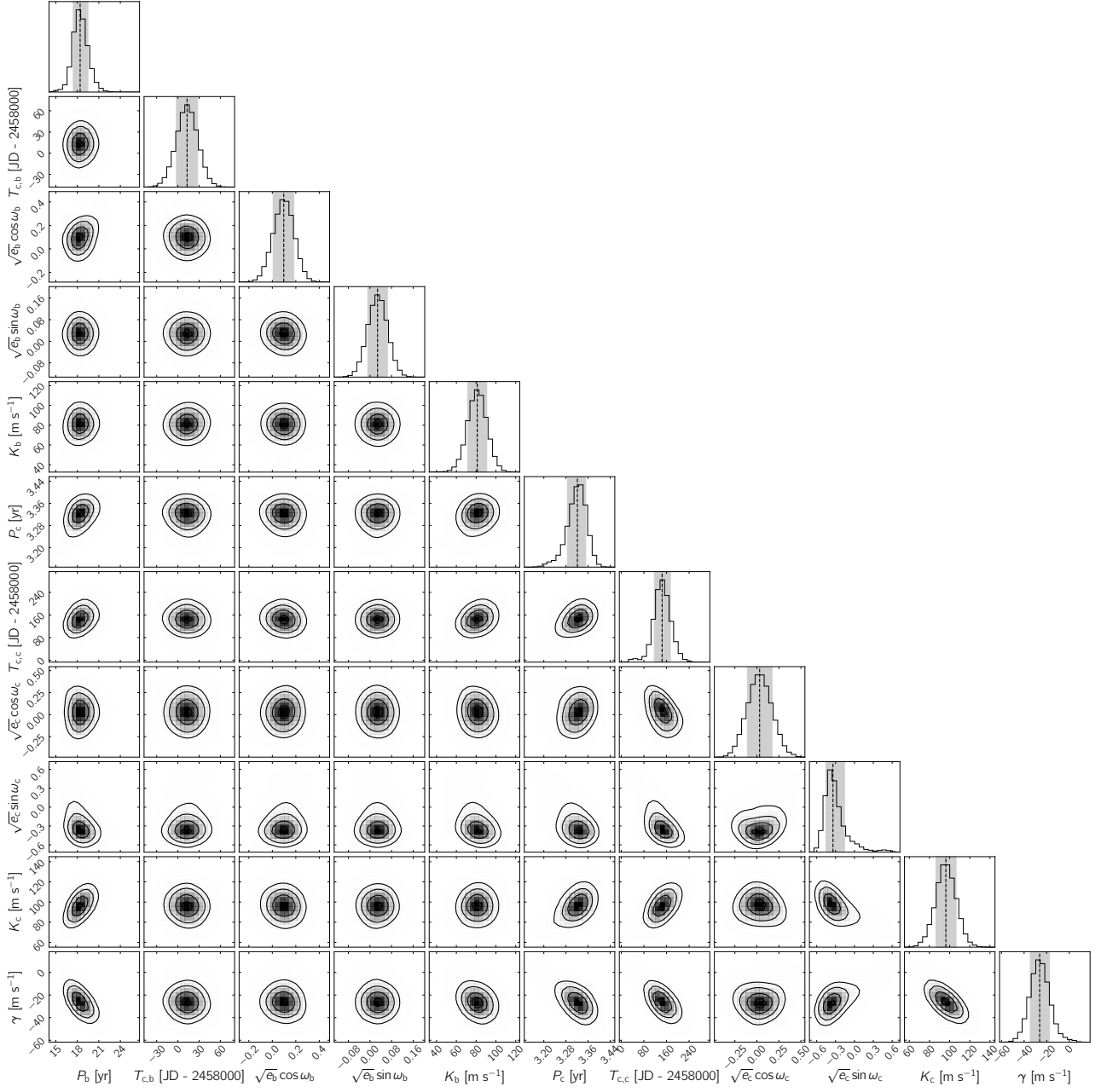


**Figure 15.** Posterior distribution of the Case C RV fit. The dashed lines and grey shaded areas show the median and the  $1\sigma$  interval for each parameter. Gaussian priors from [Lagrange et al. \(2019b\)](#) were applied on the orbital parameter of  $\beta$  Pic b, but with a wide prior of  $22 \pm 4$  yr on  $P_b$ .

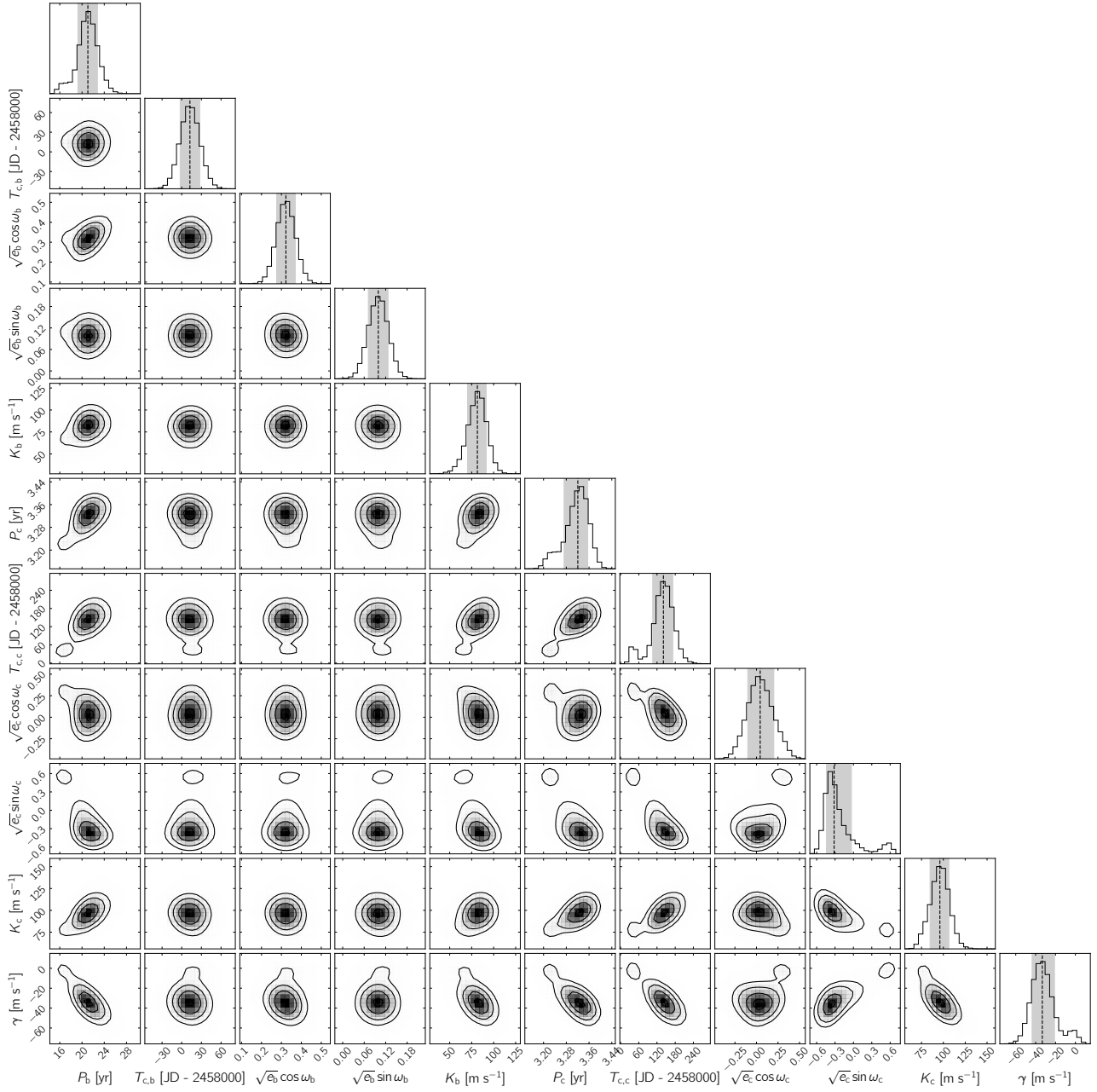


**Figure 16.** Posterior distribution of the Case D RV fit. The dashed lines and grey shaded areas show the median and the  $1\sigma$  interval for each parameter. Gaussian priors from [Nielsen et al. \(2020\)](#) were applied on the orbital parameter of  $\beta$  Pic b, but with a wide prior of  $22 \pm 4$  yr on  $P_b$ .

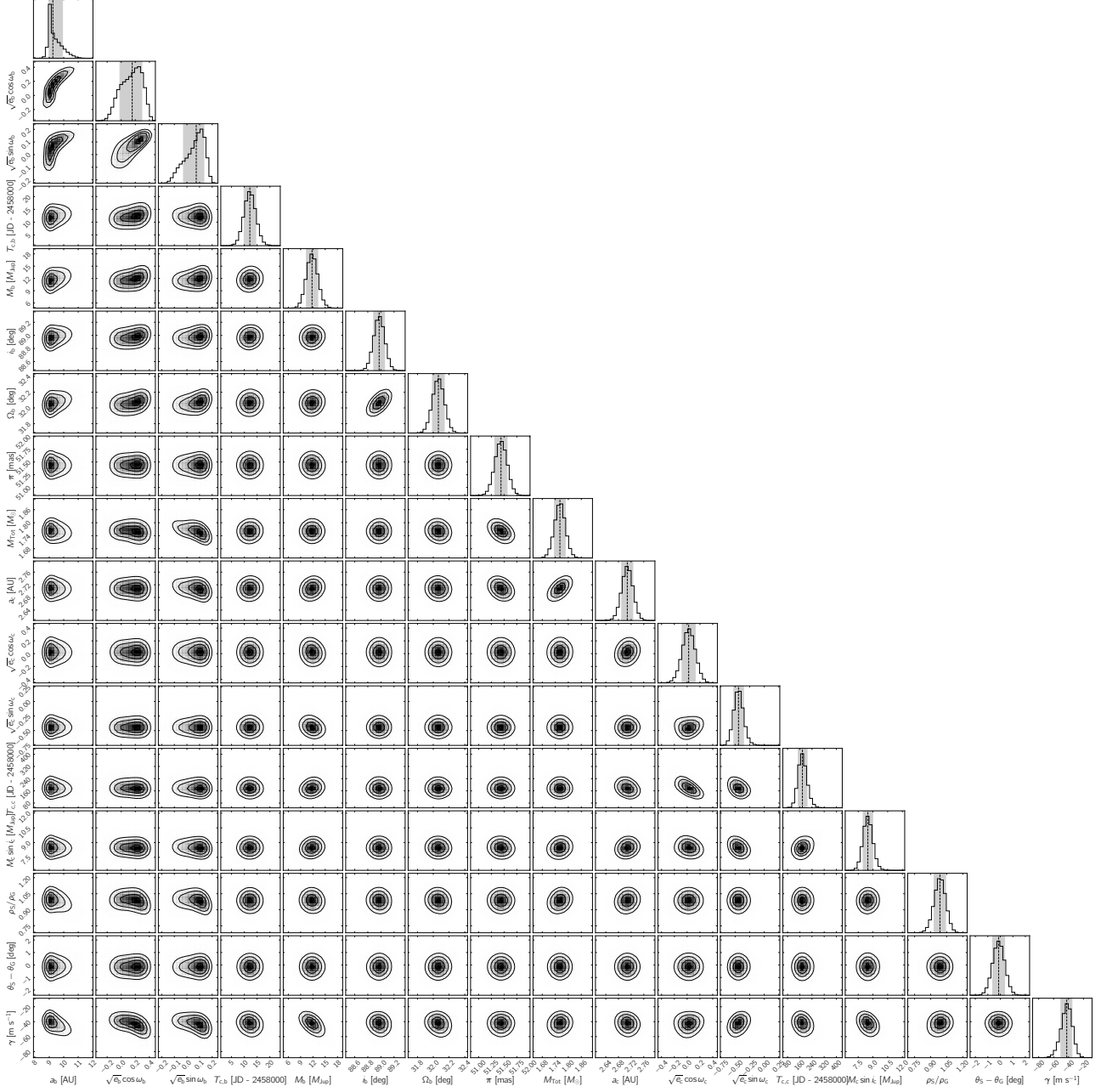


**Figure 17.** Posterior distribution for the joint fit of RV and relative astrometry, without the VLTI/GRAVITY measurement of September 2008. The dashed lines and grey shaded areas show the median and the  $1\sigma$  interval for each parameter. We note very strong correlations between  $a_b$ ,  $h_b = \sqrt{e_b} \cos \omega_b$ ,  $k_b = \sqrt{e_b} \sin \omega_b$ .

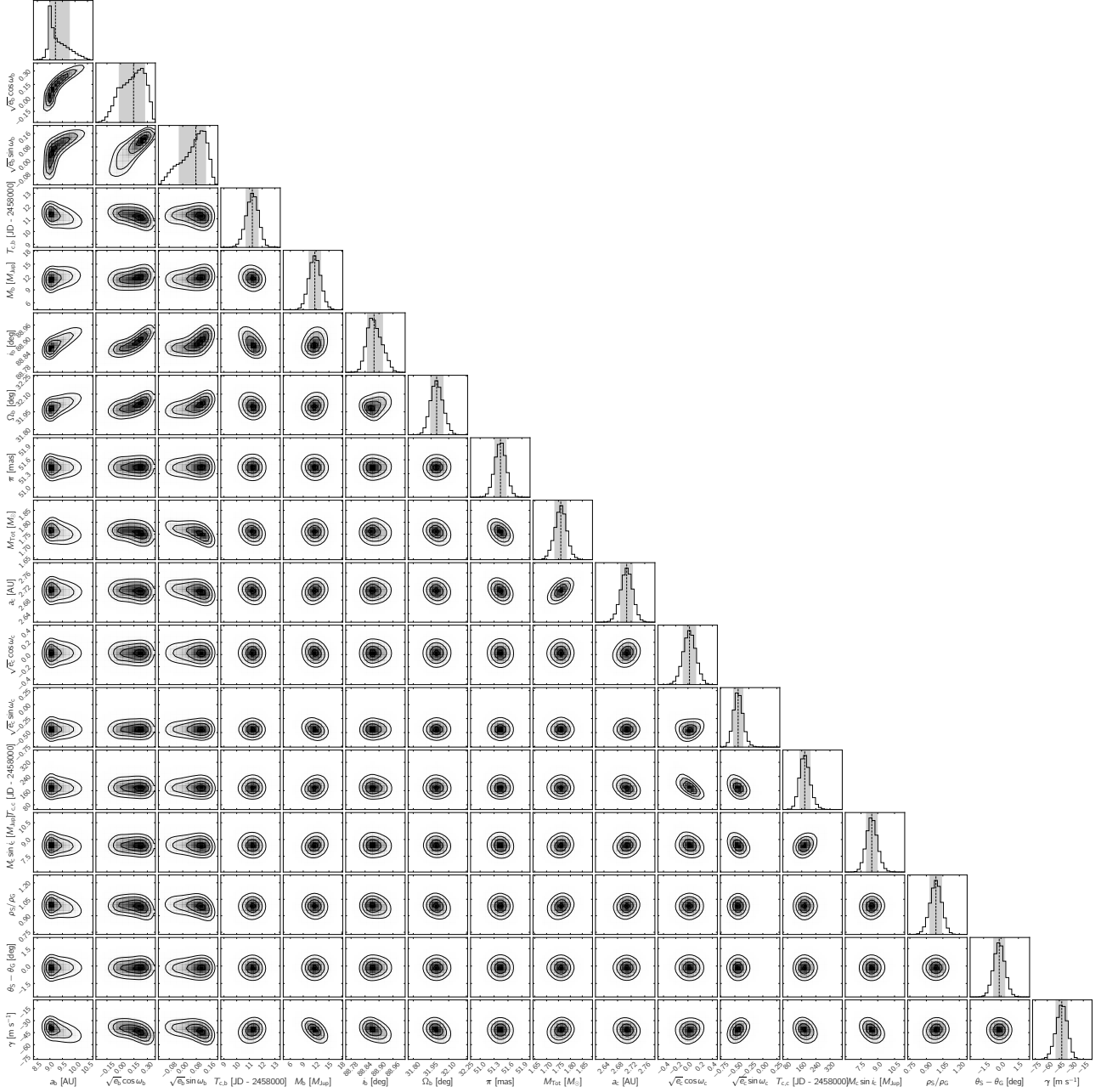


**Figure 18.** Posterior distribution for the joint fit of RV and relative astrometry, with the VLTI/GRAVITY measurement of September 2008. The dashed lines and grey shaded areas show the median and the  $1\sigma$  interval for each parameter. As in Figure 17,  $a_b$ ,  $h_b = \sqrt{e_b} \cos \omega_b$ ,  $k_b = \sqrt{e_b} \sin \omega_b$  are strongly correlated.

## B. TABLE WITH NEWLY DERIVED RV OFFSET + ERROR

**Table 3.** RV Offsets from 2003-2018.

MJD	RV	$\sigma_{\text{RV}}$
	[m s <sup>-1</sup> ]	[m s <sup>-1</sup> ]
52944.376672	-77.43	59.87
52993.188574	39.68	28.94
53048.602259	-154.64	34.06
53775.641184	-9.07	149.54
54056.325773	20.93	106.71
54112.579919	-99.04	247.39
54441.746852	-191.08	148.94
54483.110698	-92.49	135.89
54544.046717	-76.74	16.72
54780.215069	-70.24	24.16
54799.213508	-71.54	25.30
54829.165935	-202.14	27.49
54850.142609	-130.78	22.24
54913.040806	-84.29	18.44
55131.298795	2.44	26.38
55170.202032	18.54	22.49
55519.296681	37.59	30.68
55566.194698	148.72	14.54
55597.126002	85.80	19.29
56569.311461	129.29	41.54
56582.333626	95.49	28.91
56685.203668	24.62	32.80
56694.067479	91.60	27.57
56706.582371	198.96	23.64
56984.282332	-15.44	20.36
57344.247022	-148.18	55.92
57667.303333	106.83	22.29
57712.283914	128.33	21.42
57771.166012	81.25	8.54
57849.014450	151.55	25.00
58007.347048	3.42	21.89
58037.271945	37.74	7.34
58064.265248	-62.63	24.20
58094.192294	-35.32	6.94
58207.056451	-32.82	11.04
58235.001291	-70.57	7.73



## REFERENCES

- Ahmic, M., Croll, B., & Artymowicz, P. 2009, *The Astrophysical Journal*, 705, 529, doi: [10.1088/0004-637X/705/1/529](https://doi.org/10.1088/0004-637X/705/1/529)
- Angus, R., Morton, T., Aigrain, S., Foreman-Mackey, D., & Rajpaul, V. 2018, *Monthly Notices of the Royal Astronomical Society*, 474, 2094, doi: [10.1093/mnras/stx2109](https://doi.org/10.1093/mnras/stx2109)
- Baraffe, I., Chabrier, G., Barman, T. S., Allard, F., & Hauschildt, P. H. 2003, *Astronomy & Astrophysics*, 402, 701, doi: [10.1051/0004-6361:20030252](https://doi.org/10.1051/0004-6361:20030252)
- Baraffe, I., Homeier, D., Allard, F., & Chabrier, G. 2015, *Astronomy & Astrophysics*, 577, A42, doi: [10.1051/0004-6361/201425481](https://doi.org/10.1051/0004-6361/201425481)
- Bell, C. P. M., Rees, J. M., Naylor, T., et al. 2014, *Monthly Notices of the Royal Astronomical Society*, 445, 3496, doi: [10.1093/mnras/stu1944](https://doi.org/10.1093/mnras/stu1944)
- Beust, H., Lagrange, A.-M., Crawford, I. A., et al. 1998, *Astronomy and Astrophysics*, 338, 1015. <http://adsabs.harvard.edu/abs/1998A%26A...338.1015B>
- Beust, H., Lagrange-Henri, A. M., Madjar, A. V., & Ferlet, R. 1990, *Astronomy and Astrophysics*, 236, 202. <http://adsabs.harvard.edu/abs/1990A%26A...236..202B>
- Beust, H., & Morbidelli, A. 1996, *Icarus*, 120, 358, doi: [10.1006/icar.1996.0056](https://doi.org/10.1006/icar.1996.0056)
- Blunt, S., Wang, J. J., Angelo, I., et al. 2020, *The Astronomical Journal*, 159, 89, doi: [10.3847/1538-3881/ab6663](https://doi.org/10.3847/1538-3881/ab6663)
- Bowler, B. P., Liu, M. C., Shkolnik, E. L., & Tamura, M. 2014, *The Astrophysical Journal Supplement Series*, 216, 7, doi: [10.1088/0067-0049/216/1/7](https://doi.org/10.1088/0067-0049/216/1/7)
- Brown, A. G. A., Vallenari, A., Prusti, T., et al. 2018, *Astronomy & Astrophysics*, 616, A1, doi: [10.1051/0004-6361/201833051](https://doi.org/10.1051/0004-6361/201833051)
- Burrows, C. J., Krist, J. E., Stapelfeldt, K. R., & WFPC2 Investigation Definition Team. 1995, 187, 32.05. <http://adsabs.harvard.edu/abs/1995AAS...187.3205B>
- Chauvin, G., Lagrange, A.-M., Beust, H., et al. 2012, *Astronomy & Astrophysics*, 542, A41, doi: [10.1051/0004-6361/201118346](https://doi.org/10.1051/0004-6361/201118346)
- Chilcote, J., Pueyo, L., Rosa, R. J. D., et al. 2017, *The Astronomical Journal*, 153, 182, doi: [10.3847/1538-3881/aa63e9](https://doi.org/10.3847/1538-3881/aa63e9)
- Cloutier, R., Doyon, R., Menou, K., et al. 2017a, *The Astronomical Journal*, 153, 9, doi: [10.3847/1538-3881/153/1/9](https://doi.org/10.3847/1538-3881/153/1/9)
- Cloutier, R., Astudillo-Defru, N., Doyon, R., et al. 2017b, *Astronomy & Astrophysics*, 608, A35, doi: [10.1051/0004-6361/201731558](https://doi.org/10.1051/0004-6361/201731558)
- Crepp, J. R., Johnson, J. A., Howard, A. W., et al. 2012, *The Astrophysical Journal*, 761, 39, doi: [10.1088/0004-637X/761/1/39](https://doi.org/10.1088/0004-637X/761/1/39)
- Crouzet, N., Chapellier, E., Guillot, T., et al. 2018, *Astronomy & Astrophysics*, 619, A116, doi: [10.1051/0004-6361/201732565](https://doi.org/10.1051/0004-6361/201732565)
- Currie, T., Lada, C. J., Plavchan, P., et al. 2009, *The Astrophysical Journal*, 698, 1, doi: [10.1088/0004-637X/698/1/1](https://doi.org/10.1088/0004-637X/698/1/1)
- Currie, T., Thalmann, C., Matsumura, S., et al. 2011, *The Astrophysical Journal Letters*, 736, L33, doi: [10.1088/2041-8205/736/2/L33](https://doi.org/10.1088/2041-8205/736/2/L33)
- Dent, W. R. F., Thi, W. F., Kamp, I., et al. 2013, *Publications of the Astronomical Society of the Pacific*, 125, 477, doi: [10.1086/670826](https://doi.org/10.1086/670826)
- Dupuy, T. J., Brandt, T. D., Kratter, K. M., & Bowler, B. P. 2019, *The Astrophysical Journal*, 871, L4, doi: [10.3847/2041-8213/aafb31](https://doi.org/10.3847/2041-8213/aafb31)
- Dupuy, T. J., & Liu, M. C. 2017, *The Astrophysical Journal Supplement Series*, 231, 15, doi: [10.3847/1538-4365/aa5e4c](https://doi.org/10.3847/1538-4365/aa5e4c)
- Ford, E. B. 2006, *The Astrophysical Journal*, 642, 505, doi: [10.1086/500802](https://doi.org/10.1086/500802)
- Foreman-Mackey, D. 2016, *corner.py: Scatterplot matrices in Python*, doi: [10.21105/joss.00024](https://doi.org/10.21105/joss.00024)
- Foreman-Mackey, D., Agol, E., Ambikasaran, S., & Angus, R. 2017, *The Astronomical Journal*, 154, 220, doi: [10.3847/1538-3881/aa9332](https://doi.org/10.3847/1538-3881/aa9332)
- Foreman-Mackey, D., Hogg, D. W., Lang, D., & Goodman, J. 2013, *Publications of the Astronomical Society of the Pacific*, 125, 306, doi: [10.1086/670067](https://doi.org/10.1086/670067)
- Fulton, B. J., Petigura, E. A., Blunt, S., & Sinukoff, E. 2018, *Publications of the Astronomical Society of the Pacific*, 130, 044504, doi: [10.1088/1538-3873/aaaaa8](https://doi.org/10.1088/1538-3873/aaaaa8)
- Galland, F., Lagrange, A.-M., Udry, S., et al. 2005, *Astronomy & Astrophysics*, 443, 337, doi: [10.1051/0004-6361:20052938](https://doi.org/10.1051/0004-6361:20052938)
- Golimowski, D. A., Ardila, D. R., Krist, J. E., et al. 2006, *The Astronomical Journal*, 131, 3109, doi: [10.1086/503801](https://doi.org/10.1086/503801)
- Gray, R. O., Corbally, C. J., Garrison, R. F., et al. 2006, *The Astronomical Journal*, 132, 161, doi: [10.1086/504637](https://doi.org/10.1086/504637)
- Grunblatt, S. K., Howard, A. W., & Haywood, R. D. 2015, *The Astrophysical Journal*, 808, 127, doi: [10.1088/0004-637X/808/2/127](https://doi.org/10.1088/0004-637X/808/2/127)
- Hara, N. C., Boué, G., Laskar, J., Delisle, J. B., & Unger, N. 2019, *Monthly Notices of the Royal Astronomical Society*, 489, 738, doi: [10.1093/mnras/stz1849](https://doi.org/10.1093/mnras/stz1849)

- Haywood, R. D., Collier Cameron, A., Queloz, D., et al. 2014, *Monthly Notices of the Royal Astronomical Society*, 443, 2517, doi: [10.1093/mnras/stu1320](https://doi.org/10.1093/mnras/stu1320)
- Hillenbrand, L., Isaacson, H., Marcy, G., et al. 2015, in *Cambridge Workshop on Cool Stars, Stellar Systems, and the Sun*, Vol. 18, 18th Cambridge Workshop on Cool Stars, Stellar Systems, and the Sun, 759–766. <https://arxiv.org/abs/1408.3475>
- Kiefer, F., des Etangs, A. L., Boissier, J., et al. 2014, *Nature*, 514, 462, doi: [10.1038/nature13849](https://doi.org/10.1038/nature13849)
- Koen, C. 2003, *Monthly Notices of the Royal Astronomical Society*, 341, 1385, doi: [10.1046/j.1365-8711.2003.06509.x](https://doi.org/10.1046/j.1365-8711.2003.06509.x)
- Lagrange, A.-M., De Bondt, K., Meunier, N., et al. 2012a, *Astronomy & Astrophysics*, 542, A18, doi: [10.1051/0004-6361/201117985](https://doi.org/10.1051/0004-6361/201117985)
- Lagrange, A. M., Meunier, N., Chauvin, G., et al. 2013, *A&A*, 559, A83, doi: [10.1051/0004-6361/201220770](https://doi.org/10.1051/0004-6361/201220770)
- Lagrange, A.-M., Plazy, F., Beust, H., et al. 1996, *Astronomy and Astrophysics*, 310, 547. <http://adsabs.harvard.edu/abs/1996A%26A...310..547L>
- Lagrange, A.-M., Bonnefoy, M., Chauvin, G., et al. 2010, *Science*, 329, 57, doi: [10.1126/science.1187187](https://doi.org/10.1126/science.1187187)
- Lagrange, A.-M., Boccaletti, A., Milli, J., et al. 2012b, *Astronomy & Astrophysics*, 542, A40, doi: [10.1051/0004-6361/201118274](https://doi.org/10.1051/0004-6361/201118274)
- Lagrange, A.-M., Meunier, N., Rubini, P., et al. 2019a, *Nature Astronomy*, 3, 1135, doi: [10.1038/s41550-019-0857-1](https://doi.org/10.1038/s41550-019-0857-1)
- Lagrange, A.-M., Boccaletti, A., Langlois, M., et al. 2019b, *Astronomy & Astrophysics*, 621, L8, doi: [10.1051/0004-6361/201834302](https://doi.org/10.1051/0004-6361/201834302)
- Mamajek, E. E., & Bell, C. P. M. 2014, *Monthly Notices of the Royal Astronomical Society*, 445, 2169, doi: [10.1093/mnras/stu1894](https://doi.org/10.1093/mnras/stu1894)
- Mayor, M., Pepe, F., Queloz, D., et al. 2003, *The Messenger*, 114, 20
- Mékarnia, D., Chapellier, E., Guillot, T., et al. 2017, *Astronomy & Astrophysics*, 608, L6, doi: [10.1051/0004-6361/201732121](https://doi.org/10.1051/0004-6361/201732121)
- Messina, S., Lanzafame, A. C., Feiden, G. A., et al. 2016, *Astronomy & Astrophysics*, 596, A29, doi: [10.1051/0004-6361/201628524](https://doi.org/10.1051/0004-6361/201628524)
- Morzinski, K. M., Males, J. R., Skemer, A. J., et al. 2015, *The Astrophysical Journal*, 815, 108, doi: [10.1088/0004-637X/815/2/108](https://doi.org/10.1088/0004-637X/815/2/108)
- Mouillet, D., Larwood, J. D., Papaloizou, J. C. B., & Lagrange, A. M. 1997, *Monthly Notices of the Royal Astronomical Society*, 292, 896, doi: [10.1093/mnras/292.4.896](https://doi.org/10.1093/mnras/292.4.896)
- Nielsen, E. L., Liu, M. C., Wahhaj, Z., et al. 2014, *The Astrophysical Journal*, 794, 158, doi: [10.1088/0004-637X/794/2/158](https://doi.org/10.1088/0004-637X/794/2/158)
- Nielsen, E. L., Rosa, R. J. D., Wang, J., et al. 2016, *The Astronomical Journal*, 152, 175, doi: [10.3847/0004-6256/152/6/175](https://doi.org/10.3847/0004-6256/152/6/175)
- Nielsen, E. L., Rosa, R. J. D., Wang, J. J., et al. 2020, *The Astronomical Journal*, 159, 71, doi: [10.3847/1538-3881/ab5b92](https://doi.org/10.3847/1538-3881/ab5b92)
- Nowak, M., Lacour, S., Mollière, P., et al. 2020, *Astronomy & Astrophysics*, 633, A110, doi: [10.1051/0004-6361/201936898](https://doi.org/10.1051/0004-6361/201936898)
- Rajpaul, V., Aigrain, S., Osborne, M. A., Reece, S., & Roberts, S. 2015, *Monthly Notices of the Royal Astronomical Society*, 452, 2269, doi: [10.1093/mnras/stv1428](https://doi.org/10.1093/mnras/stv1428)
- Ryu, T., Sato, B., Kuzuhara, M., et al. 2016, *The Astrophysical Journal*, 825, 127, doi: [10.3847/0004-637X/825/2/127](https://doi.org/10.3847/0004-637X/825/2/127)
- Smith, B. A., & Terrile, R. J. 1984, *Science*, 226, 1421, doi: [10.1126/science.226.4681.1421](https://doi.org/10.1126/science.226.4681.1421)
- Snellen, I. A. G., Brandl, B. R., de Kok, R. J., et al. 2014, *Nature*, 509, 63, doi: [10.1038/nature13253](https://doi.org/10.1038/nature13253)
- Snellen, I. A. G., & Brown, A. G. A. 2018, *Nature Astronomy*, 2, 883, doi: [10.1038/s41550-018-0561-6](https://doi.org/10.1038/s41550-018-0561-6)
- Soderblom, D. R., Hillenbrand, L. A., Jeffries, R. D., Mamajek, E. E., & Naylor, T. 2014, in *Protostars and Planets VI*, ed. H. Beuther, R. S. Klessen, C. P. Dullemond, & T. Henning, 219, doi: [10.2458/azu\\_uapress.9780816531240-ch010](https://doi.org/10.2458/azu_uapress.9780816531240-ch010)
- Spiegel, D. S., & Burrows, A. 2012, *The Astrophysical Journal*, 745, 174, doi: [10.1088/0004-637X/745/2/174](https://doi.org/10.1088/0004-637X/745/2/174)
- The Astropy Collaboration, Robitaille, T. P., Tollerud, E. J., et al. 2013, *Astronomy & Astrophysics*, 558, A33, doi: [10.1051/0004-6361/201322068](https://doi.org/10.1051/0004-6361/201322068)
- van Leeuwen, F. 2007, *Astronomy and Astrophysics*, 474, 653, doi: [10.1051/0004-6361:20078357](https://doi.org/10.1051/0004-6361:20078357)
- Wang, J. J., Graham, J. R., Pueyo, L., et al. 2016, *The Astronomical Journal*, 152, 97, doi: [10.3847/0004-6256/152/4/97](https://doi.org/10.3847/0004-6256/152/4/97)
- Zieba, S., Zwintz, K., Kenworthy, M. A., & Kennedy, G. M. 2019, *Astronomy & Astrophysics*, 625, L13, doi: [10.1051/0004-6361/201935552](https://doi.org/10.1051/0004-6361/201935552)
- Zuckerman, B., Song, I., Bessell, M. S., & Webb, R. A. 2001, *The Astrophysical Journal Letters*, 562, L87, doi: [10.1086/337968](https://doi.org/10.1086/337968)
- Zwintz, K., Reese, D. R., Neiner, C., et al. 2019, *Astronomy & Astrophysics*, 627, A28, doi: [10.1051/0004-6361/201834744](https://doi.org/10.1051/0004-6361/201834744)